The Astrophysical Journal, 982:171 (17pp), 2025 April 1 https://doi.org/10.3847/1538-4357/adb8ca

DIISC-VI (COS-DIISC): Ultraviolet Metal Absorption Relative to the H I Disk of Galaxies

Brad Koplitz[1], Sanchayeeta Borthakur[1], Timothy Heckman[1,2], Mansi Padave[1], Tyler McCabe[1], Jason Tumlinson[3], Andrew J. Fox[4,5], and Guinevere Kauffmann[6]
[1] School of Earth & Space Exploration, Arizona State University, 781 Terrace Mall, Tempe, AZ 85287, USA; Brad.Koplitz@asu.edu
[2] Department of Physics & Astronomy, Johns Hopkins University, Bloomberg Centre, 3400 N. Charles Street, Baltimore, MD 21218, USA
[3] Space Telescope Science Institute, 3700 San Martin Drive, Baltimore, MD, USA
[4] AURA for ESA, Space Telescope Science Institute, 3700 San Martin Drive, Baltimore, MD 21218, USA
[5] Department of Physics & Astronomy, Johns Hopkins University, 3400 N. Charles Street, Baltimore, MD 21218, USA
[6] Max-Planck-Institute für Astrophysik, Karl-Schwarzschild-Str 1, D-85740 Garching, Germany
Received 2024 August 21; revised 2025 January 17; accepted 2025 February 3; published 2025 March 27

Abstract

As part of the Deciphering the Interplay between the Interstellar medium, Stars, and the Circumgalactic medium (DIISC) survey, we present the UV metal absorption features in the circumgalactic medium (CGM) near the H I gas disk ($<4.5R_{\rm HI}$) of 31 nearby galaxies through quasar absorption-line spectroscopy. Of the ions under study, Si IIIλ1206 was most frequently detected (18 of 31 sight lines), while C IIλ1334 and Si IIλ1260 were detected in 17 and 15 of 31 sight lines, respectively. Many components were consistent with photoionization equilibrium models; most of the cold and cool gas phase clouds were found to have lengths smaller than 2 kpc. Sight lines with smaller impact parameters (ρ) normalized by the galaxy's virial radius ($R_{\rm vir}$) and H I radius ($R_{\rm HI}$) tend to have more components and larger rest-frame equivalent widths (W_r) than those that probe the CGM at larger radii. In particular, we find that the location of metals are better traced by $\rho/R_{\rm HI}$ rather than the traditional $\rho/R_{\rm vir}$. Larger covering fractions are found closer to galaxies, with a radial decline that depends on the W_r limit used. Our results provide new insights into the spatial distribution of metals around the H I disks of low-redshift galaxies.

Unified Astronomy Thesaurus concepts: Photoionization (2060); Quasar-galaxy pairs (1316); Quasar absorption line spectroscopy (1317)

Materials only available in the online version of record: figure sets, machine-readable tables

1. Introduction

The halo gas associated with galaxies extends well beyond where we see stars. It is known that this medium, referred to as the circumgalactic medium (CGM), is multiphase and can be found out to and beyond the virial radius of galaxies ($R_{\rm vir}$; J. Tumlinson et al. 2017 and references therein). This gas is fundamental to understanding how galaxies evolve as it is a major component of their baryon cycles (C. Péroux & J. C. Howk 2020; M. Donahue & G. M. Voit 2022). Star formation is thought to be triggered from gas accreting from the CGM and the intergalactic medium (e.g., D. Kereš et al. 2005; A. Dekel & Y. Birnboim 2006; A. Dekel et al. 2009; R. S. Somerville & R. Davé 2015; Z. Hafen et al. 2022; D. Decataldo et al. 2023), while feedback mechanisms, such as stellar winds, return this gas back to the CGM (e.g., S. Veilleux et al. 2005; S. Shen et al. 2012; J. Suresh et al. 2015; C.-A. Faucher-Giguère et al. 2016; G. Kauffmann et al. 2016; R. E. G. Machado et al. 2018; J. J. Davies et al. 2020; D. Sorini et al. 2020; G. M. Voit et al. 2020; E. Zinger et al. 2020).

There are numerous benefits to studying the metal absorbers in the CGM. They often show multiple components even when the associated Lyα is saturated or damped (e.g., H. W. Chen et al. 2002; J. K. Werk et al. 2013; R. Bordoloi et al. 2014; S. Borthakur et al. 2016; B. A. Keeney et al. 2017; S. Muzahid et al. 2018), allowing the column densities and Doppler widths of absorbers to be measured more precisely. Metals also probe the multiple phases of the CGM (e.g., J. K. Werk et al. 2013; K. J. Haislmaier et al. 2021; Sameer et al. 2024), enabling the ionization state around galaxies to be constrained. Additionally, the physical size of these CGM absorbing clouds can be estimated by comparing ionization models to observed metal lines (e.g., J. T. Stocke et al. 2013; J. K. Werk et al. 2014; S. Muzahid et al. 2018).

The Cosmic Origins Spectrograph (COS)-Halos survey (J. Tumlinson et al. 2013) studied the CGM around 44 $L_\star$ galaxies, both passive and star-forming, at redshifts of $z \approx 0.2$. In particular, at least one line from intermediate ions was found in 75% of systems. This suggested the presence of a cool ($T \sim 10^4$–10^5 K), metal-rich CGM component around most galaxies (J. K. Werk et al. 2013). The strength of the metal absorbers was found to decrease with increasing impact parameter (ρ), implying a decreasing metal surface density profile. This radial decline has been reproduced by simulations (e.g., S. Appleby et al. 2021). Both star-forming and quenched galaxies were found to have CGM masses of $\sim 10^{10}$ $M_\odot$, meaning the early types have less CGM mass relative to their stellar and halo masses as compared to star-forming galaxies, which may be a signature of quenching (C. Thom et al. 2012). Additionally, the quenching of star formation was found to take place regardless of the presence of strong H I absorption, contrary to some theoretical expectations (C. Thom et al. 2012). However, J. N. Burchett et al. (2018) found that the CGM of X-ray-bright clusters contained less H I relative to field galaxies, which may be indicative of quenching. More recently, K. Tchernyshyov et al. (2023) found that star-forming galaxies

tend to have more O VI in their CGM than passive galaxies at the same stellar mass.

Rather than statistically studying many CGMs probed by single QSOs, B. A. Keeney et al. (2013) investigated a single galaxy (ESO 157-49) using three sight lines, a subsample of 11 sight lines in the catalog of J. T. Stocke et al. (2013). The two sight lines probing along the disk of the edge-on galaxy contained absorption from Si III, C IV, and Si IV. These absorbers provided further evidence that the warm phase of the CGM have high covering fractions, similar to what was found by J. Tumlinson et al. (2011). The sight line near the galaxy's minor axis only showed detection of H I; however, it is worth noting that this sight line is located at nearly twice the virial radius of the galaxy. Using these sight lines, along with the full sample from J. T. Stocke et al. (2013) and a subsample of the C. W. Danforth & J. M. Shull (2008) catalog, B. A. Keeney et al. (2017) found that the CGM of star-forming galaxies likely contains a few thousand cool clouds with sizes between 1 and 20 kpc, with many more at sizes between 200 pc and 1 kpc. These cloud sizes, including some as small as 10 pc, have been found by J. R. Rigby et al. (2002) and the Cosmic Ultraviolet Baryon Survey (CUBS; F. S. Zahedy et al. 2021).

In a similar study, D. V. Bowen et al. (2016) used four QSO sight lines to study the CGM of NGC 1097. The three sight lines closest to the galaxy contained Si III, while Si II, C II, and Si IV were only found along the closest sight line. The dearth of Si IV detections suggests that the warm phase may not be as prevalent as was found by J. Tumlinson et al. (2011) and B. A. Keeney et al. (2013).

The Galaxy Evolution Explorer (GALEX) Arecibo Sloan Digital Sky Survey (GASS) looked at Lyα absorption features in the outer CGM of 36 far-ultraviolet (FUV) bright QSO–galaxy pairs (S. Borthakur et al. 2015). The strength of Lyα absorption was found to sharply drop at $\rho \approx 136$ kpc, even when normalized by the target galaxy's $R_{\rm vir}$. A similar decline has been seen by other surveys (e.g., B. A. Keeney et al. 2017; M. C. Wilde et al. 2021; V. V. Klimenko et al. 2023) and in simulations (e.g., F. van de Voort et al. 2019; D. Nelson et al. 2020). Stronger Lyα absorption was also found to be positively correlated with larger H I mass in the galaxy's interstellar medium (ISM). No correlation was observed, however, between Lyα absorption and the galaxy's stellar mass or orientation with respect to its optical major axis. These imply that Lyα absorbers are able to trace the CGM structure around galaxies.

The combined COS-Halos + GASS sample found almost no Si III beyond $\sim$0.8 $R_{\rm vir}$ (S. Borthakur et al. 2016). A positive correlation was seen, though, between the galaxy's star formation rate (SFR) and rest-frame equivalent width (W_r) of both Lyα and Si III. The kinematic properties of the sample showed no dependence on the galaxy's halo mass; thus, gravity alone cannot explain the observed dynamics. These further indicated that Si III and Lyα may be in the same physical regions, as was shown by P. Richter et al. (2016).

Motivated by the discovery of COS-GASS that a galaxy's H I mass and the strength of W_r(Lyα) in its CGM are correlated (S. Borthakur et al. 2015, 2016), we have designed the Deciphering the Interplay between the ISM, Stars, and the CGM (DIISC) survey to trace the entire baryon cycle in the local Universe (H. B. Gim et al. 2021; M. Padave et al. 2021, 2024a, 2024b; S. Borthakur et al. 2024). We add to the survey by investigating the CGM absorption features in the sample, which we refer to as COS-DIISC. Here, we focus on the metal absorbers, while the Lyα features, as well as a complete discussion of the survey design and goals, are discussed in S. Borthakur et al. (2024).

There have been many absorption-line spectroscopic surveys that have characterized the CGM across a range of galaxy properties and redshifts (e.g., KBSS, G. C. Rudie et al. 2012; COS-Halos, J. Tumlinson et al. 2013; COS-Dwarfs, R. Bordoloi et al. 2014; COS-GASS, S. Borthakur et al. 2015; COS-Burst, T. Heckman et al. 2017; COS-Weak, S. Muzahid et al. 2018; CASBaH, J. N. Burchett et al. 2019; CUBS, H.-W. Chen et al. 2020; Project AMIGA, N. Lehner et al. 2020; CGM^2, M. C. Wilde et al. 2021). The COS-DIISC program continues this by investigating the kinematics, content, and ionization state of the gas at the disk–CGM interface of galaxies as never before.

The rest of the paper is outlined as follows. Section 2 details the DIISC sample, the observations used in our analysis, and how we identified lines in our spectra. Our analysis is described in Section 3. Finally, Section 4 summarizes our results and main conclusions. Throughout this paper, we assume a cosmology with $H_0 = 70\,{\rm km\,s^{-1}}$ Mpc^{-1}, $\Omega_m = 0.3$, and $\Omega_\Lambda = 0.7$.

2. Sample and Data

2.1. The DIISC Sample

The DIISC survey selected all galaxies with an FUV bright QSO (GALEX FUV magnitude brighter than 19) within $\sim$3.5 times their H I radii ($R_{\rm HI}$),[7] as calculated from the ALFALFA survey (R. Giovanelli et al. 2005; M. P. Haynes et al. 2018) and the HIPASS survey (M. J. Meyer et al. 2004; M. A. Zwaan et al. 2004). This led to a complete sample of 32 QSOs probing 34 local foreground galaxies. For four galaxies, further observations revealed smaller H I radii than were found by the ALFALFA and HIPASS surveys, meaning their background QSOs probe the galaxies between 3.5 and 4.5 $R_{\rm HI}$.

We exclude two sight lines from the final sample. J0235 −0925 was excluded because the data quality of the UV spectrum was too poor for fits to be performed. In addition, J1024+2422 was excluded because of the presence of a Lyman limit system at a redshift of $z \approx 0.525$, leaving no flux below $\sim$1391 Å. This makes Si IV the only available species, which we did not detect. We also exclude the galaxy KUG 1429+101 (probed by QSO J1432+0955) since it is at the same z as NGC 5669 but with less mass and smaller radii; thus, we attribute the observed absorption to the larger galaxy. This leaves 30 QSOs probing 31 foreground galaxies in the final sample.

The left panel of Figure 1 shows the distribution of stellar mass ($M_\star$) of our sample, while the right panel indicates the impact parameter of the background QSOs normalized by the radius of the galaxy's $R_{\rm HI}$. The DIISC galaxies cover a range of $M_\star$, $\log(M_\star/M_\odot) = 8.5$–$12.0$, and have specific SFRs (sSFR $\equiv$ SFR$/M_\star$) between $10^{-12.05}$–$10^{-9.96}\,{\rm yr^{-1}}$. Similarly, we cover a large range of impact parameters, $\rho = 21$–163 kpc. The properties of the COS-DIISC sample are listed in Table 1.

[7] The H I radius of a galaxy is defined as the mean radius with a mass surface density $\Sigma(M_{\rm HI}) = 1\ M_\odot\,{\rm pc^{-2}}$.

Table 1
Properties of the DIISC Sample

QSO (1)	R.A. (2)	Decl. (3)	z_{QSO} (4)	Galaxy (5)	z_{sys} (6)	ρ (7)	R_{vir} (8)	M_{halo} (9)	R_{HI} (10)	M_{HI} (11)	$M_{\star}$ (12)	sSFR (13)
J0023+1547	5.878	15.796	0.4112	NGC 99	0.0177	163	207	11.7	52.0	10.4	10.6	−10.23
J0832+2431	128.084	24.517	1.2996	KUG 0829+246B	0.0432	41	173	11.5	33.4	10.0	10.4	−10.30
J0835+2459	128.899	24.995	0.3299	NGC 2611	0.0175	55	207	12.0	20.2	9.6	10.6	−9.96
J0917+2719	139.369	27.331	0.0757	J0917+2720	0.0469	52	203	12.0	26.8	9.8	10.6	−10.88
J1042+2501	160.672	25.023	0.3426	NGC 3344	0.0020	31	165	11.4	16.8	9.4	10.2	−10.52
J1043+1151	160.900	11.858	0.7925	M95/NGC 3351	0.0026	29	334	12.3	9.7	9.0	10.9	−11.00
J1052+1017	163.086	10.298	0.2462	NGC 3433	0.0091	128	252	12.0	41.0	10.2	10.8	−10.77
J1059+1441	164.938	14.695	0.6306	NGC 3485	0.0048	83	188	11.6	24.7	9.8	10.4	−10.53
J1059+2517	164.995	25.286	0.6620	2MASXJ1059+2516	0.0207	38	145	11.3	14.6	9.3	9.9	−10.09
J1124+1131	171.165	11.521	0.1429	NGC 3666	0.0035	56	174	11.8	16.9	9.4	10.3	−10.80
J1133+2423	173.358	24.391	0.5347	NGC 3728	0.0232	120	382	12.8	68.8	10.6	11.3	−10.84
J1134+2555	173.740	25.925	0.7098	AGC 723761	0.0321	51	150	11.3	20.5	9.6	10.0	−10.99
J1140+1136	175.192	11.614	0.6871	NGC 3810	0.0033	41	187	11.6	16.7	9.4	10.4	−10.34
J1144+0705	176.145	7.088	0.0749	J1144+0703	0.0507	125	385	12.3	47.9	10.3	11.1	−11.06
J1157+0906	179.291	9.102	0.3045	AGC 213643	0.0367	88	139	11.2	33.3	10.0	9.8	−10.60
J1157+1140	179.344	11.678	0.2905	2MASXJ1157+1139	0.0213	45	146	11.6	19.0	9.5	9.9	−10.16
J1209+2616	182.322	26.270	0.5770	UGC 7138	0.0072	37	119	11.0	11.2	9.1	9.2	−10.14
J1221+0430	185.408	4.507	0.0947	M61/NGC 4303	0.0052	26	457	12.7	28.9	9.9	11.4	−10.67
J1223+1545	185.879	15.752	0.0806	M100/NGC 4321	0.0053	39	204	11.7	15.6	9.4	10.6	−10.18
J1231+1203	187.805	12.052	0.1162	IC 3440	0.0260	83	163	11.4	24.2	9.7	10.2	−10.53
J1301+2751	195.367	27.852	0.2425	NGC 4921	0.0182	53	1009	13.8	12.6	9.2	11.8	−12.05
J1303+2633	195.941	26.554	0.4356	UGC 8161	0.0223	99	240	12.2	30.4	9.9	10.8	−10.83
J1314+2606	198.696	26.107	0.0716	J1314+2605	0.0431	96	215	12.1	33.1	10.0	10.7	−10.27
J1354+1441	208.609	14.698	0.2143	KUG 1352+149	0.0418	84	213	11.8	47.1	10.3	10.7	−10.54
J1415+0445	213.775	4.763	0.2413	UGC 9120	0.0192	90	323	12.3	22.0	9.7	11.1	−10.98
J1432+0955	218.070	9.922	0.7663	NGC 5669	0.0046	29	130	11.1	13.0	9.2	9.5	−10.06
J1524+0419	231.199	4.322	0.7104	2MASXJ1524+0421	0.0374	107	221	12.1	25.5	9.8	10.7	−10.39
J1533+1501	233.310	15.017	0.0909	LEDA 140527	0.0429	22	149	11.3	24.9	9.8	10.0	−10.33
J1533+1501	233.310	15.017	0.0909	NGC 5951	0.0059	55	158	11.4	18.7	9.5	10.1	−10.74
J1558+1205	239.591	12.093	0.5745	IC 1149	0.0156	67	239	11.9	23.3	9.7	10.8	−10.75
J1558+1255	239.731	12.932	0.2879	KUG 1556+130	0.0347	109	176	11.8	30.5	9.9	10.4	−10.59

Note. Column (1) contains the GALEX name of the background QSO. Columns (2) and (3) show the R.A. and decl. (J2000) of the QSO. Column (4) indicates the QSO's redshift. Columns (5) and (6) show the name of the target galaxy and associated redshift, respectively. Column (7) is the impact parameter of the sight line in units of kiloparsec. Columns (8) and (9) have the galaxy's virial radius in kpc and its halo mass in units of log $M_{\odot}$, respectively. The halo mass was calculated using Equation (21) from P. S. Behroozi et al. (2010). Columns (10) and (11) indicate the galaxy's H I radius and mass in units of kiloparsec and log $M_{\odot}$, respectively. The H I mass was measured by the ALFALFA survey (R. Giovanelli et al. 2005; M. P. Haynes et al. 2018), with the radius being derived from the H I mass to radius relation found by R. A. Swaters et al. (2002). Column (12) is the galaxy's stellar mass in units of log $M_{\odot}$. Column (13) has the sSFR (SFR/$M_{\star}$) in units of log yr^{-1} (M. Padave et al. 2024a).

(This table is available in its entirety in machine-readable form in the online article.)

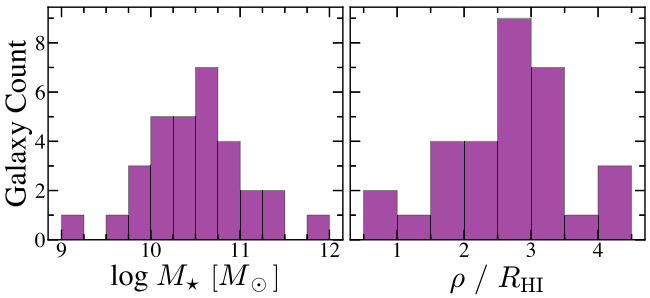

Figure 1. Distribution of stellar mass (left) and impact parameter relative to the H I radius of the targeted foreground galaxies (right) in the COS-DIISC sample.

2.2. Observations and Line Identification

The observations used in our analysis were taken with the COS (S. Osterman et al. 2011; J. C. Green et al. 2012) on board the Hubble Space Telescope (HST) through proposal GO-14071 (PI: S. Borthakur). We used the medium-resolution grating G130M ($R \approx 15{,}000$; FWHM $\approx 20\,\mathrm{km\,s^{-1}}$), which has a wavelength coverage of 1140–1470 Å. Our galaxies reside at $z \lesssim 0.05$, giving us access to FUV transitions probing a range of gas phases. These include Lyα (λ1215), O I (λ1302), Si II ($\lambda\lambda$1190, 1193, 1260, 1304), Si III (λ1206), Si IV ($\lambda\lambda$1393, 1402), C II (λ1334), and N V ($\lambda\lambda$1238, 1242). The densities and temperatures traced by these transitions can be found in Figure 6 of J. Tumlinson et al. (2017).

We used the standard COS pipeline to reduce our data set (M. Rafelski et al. 2018). Data-analysis measurements were made using the same method employed by the COS-Halos (J. Tumlinson et al. 2013; J. K. Werk et al. 2013), COS-Dwarfs (R. Bordoloi et al. 2014), and COS-GASS (S. Borthakur et al. 2015; S. Borthakur et al. 2016) surveys. Individual exposures were coadded, and the spectra was binned by 3 pixels. The COS pipeline is known to produce oversampled spectra, so binning by 3 pixels results in Nyquist sampling. The continuum of each sight line was normalized by fitting Legendre polynomials between orders 1 and 5. We identified all

Table 2
Number of Detected Components along Each Sight Line

QSO (1)	Galaxy (2)	z_{sys} (3)	O I (4)	Si II (5)	C II (6)	Si III (7)	Si IV (8)	N V (9)
J0023+1547	NGC 99	0.0177	0	0	0	0	0	0
J0832+2431	KUG 0829+246B	0.0430	2	2	1	2	⋯	0
J0835+2459	NGC 2611	0.0175	3	2	3	4	7	0
J0917+2719	J0917+2720	0.0469	1	3	2	2	⋯	0
J1042+2501	NGC 3344	0.0020	0	2	1	1	1	1
J1043+1151	M95/NGC 3351	0.0026	0	4	1	1	1	1
J1052+1017	NGC 3433	0.0091	0	0	0	0	0	0
J1059+2517	2MASXJ1059+2516	0.0207	0	0	0	0	0	0
J1059+1441	NGC 3485	0.0048	0	0	0	0	0	0
J1124+1131	NGC 3666	0.0035	0	1	2	2	2	0
J1133+2423	NGC 3728	0.0232	0	4	3	3	0	0
J1134+2555	AGC 723761	0.0321	0	0	0	0	0	0
J1140+1136	NGC 3810	0.0033	0	2	1	3	2	1
J1144+0705	J1144+0703	0.0507	0	0	0	2	⋯	⋯
J1157+0906	AGC 213643	0.0367	0	0	1	1	2	0
J1157+1140	2MASXJ1157+1139	0.0213	0	0	1	1	1	0
J1209+2616	UGC 7138	0.0072	0	0	1	0	0	0
J1221+0430	M61/NGC 4303	0.0052	2	6	5	6	7	3
J1223+1545	M100/NGC 4321	0.0053	0	0	0	0	0	0
J1231+1203	IC 3440	0.0260	0	0	0	0	0	0
J1301+2751	NGC 4921	0.0182	0	0	0	0	0	0
J1303+2633	UGC 8161	0.0223	0	0	0	0	0	0
J1314+2606	J1314+2605	0.0431	0	1	0	2	⋯	0
J1354+1441	KUG 1352+149	0.0418	0	0	0	4	⋯	0
J1415+0445	UGC 9120	0.0192	0	0	0	0	0	0
J1432+0955	NGC 5669	0.0046	2	2	2	⋯	3	0
J1524+0419	2MASXJ1524+0421	0.0374	0	1	2	2	0	0
J1533+1501	LEDA 140527	0.0429	1	2	2	3	⋯	0
J1533+1501	NGC 5951	0.0059	0	0	0	0	0	0
J1558+1205	IC 1149	0.0156	1	1	1	1	1	0
J1558+1255	KUG 1556+130	0.0347	0	0	0	0	⋯	⋯

Note. Column (1): the QSO of the sight line. Columns (2) and (3): the foreground galaxy and its redshift. Columns (4)–(9): the number of components of each ion detected at 3σ above the noise level. Ions not covered by our data are indicated by ellipses.

(This table is available in its entirety in machine-readable form in the online article.)

absorption features with rest-frame equivalent widths (W_r) at least 3σ above the noise level and within $\pm 600\,\mathrm{km\,s^{-1}}$ of the galaxy's systematic velocity (v_{sys}). The absorbers beyond $\pm 600\,\mathrm{km\,s^{-1}}$ of v_{sys} are likely not gravitationally bound to the galaxy and so are excluded in our analysis. Absorbers not associated with our target galaxies were also identified to evaluate any contamination.

2.3. Voigt Profile Analysis

Voigt profiles were fit to the absorbers in our sample to measure the velocity centroids (v_{obs}), column density (N), and Doppler width (b) of each component. Table 2 summarizes the number of detected components of each ion along the sight lines. Our rest-frame equivalent width measurements (W_r) and the results of our Voigt profile fits are presented in Table 3. For the transitions that are not detected at 3σ above the noise level, we measure W_r within $\pm 50\,\mathrm{km\,s^{-1}}$ of the galaxy's systematic velocity (v_{sys}) and report the 3σ value of the error as an upper limit. For the QSO–galaxy pair J1144+0705–J1144+0703, S II 1250 and 1253 from the Milky Way were found at the expected wavelength of Si II 1190 and 1193, respectively, of the foreground galaxy. We modeled and removed the S II lines before finding the upper limit of the Si II transitions. In some cases, there were intervening absorbers at v_{sys} that we could not model and remove from the spectra to get a more representative measurement of W_r. We note which transitions this impacted with an asterisk in Table 3.

We present an example of our analysis in Figure 2 for the QSO–galaxy pair J0835+2459–NGC 2611. The species being plotted as well as its rest wavelength, in units of angstrom, are shown in the upper left of each panel. The normalized flux and uncertainties, centered on the galaxy's v_{sys}, are shown in black and dark pink, respectively. The regions used to calculate W_r are shown in gray. Individual Voigt profile components are shown in blue, while the combined profile is in green. Any additional features within $\pm 600\,\mathrm{km\,s^{-1}}$ of the galaxy's v_{sys} are labeled as follows: Milky Way features are shown in cyan, those associated with our target galaxy are in red, those from the background QSO are yellow, while any other lines (i.e., "intervening" systems) are pink.

The QSO–galaxy pair J1042+2501–NGC 3344 was previously fit by M. Padave et al. (2021) to study the galaxy's extended UV disk. We report their measurements for H I, Si II, Si III, Si IV, and C II, rather than fitting the absorption features again due to the complex nature of the fit and low signal-to-noise values. The Voigt profile fits for this pair are shown in M. Padave et al. (2021). Most metals had a single component, while the Si II absorbers had two components. The low-z nature

Table 3
Summary of Measurements

Ion (1)	λ_{rest} (2)	W_r^a (3)	v_{obs} (4)	log$N$ (5)	b (6)
J0023+1547 at $z_{sys} = 0.0177$					
O I	1302	⩽139.5	…	⩽14.25	…
Si II	1260	⩽119.7	…	⩽12.86	…
Si II	1193	…	…	…	…
Si II	1190	⩽183.0	…	…	…
Si II	1304	⩽138.0	…	…	…
C II	1334	⩽143.1	…	⩽13.85	…
Si III	1206	⩽144.0	…	⩽12.83	…
Si IV	1393	⩽144.0	…	⩽13.21	…
Si IV	1402	⩽141.0	…	…	…
N V	1238	…[b]	…	⩽14.06	…
N V	1242	⩽123.6	…	…	…
J0832+2431 at $z_{sys} = 0.0431$					
O I	1302	69.0 ± 21.1	−41.2 ± 3.3	13.73 ± 0.05	33.1 ± 1.2
		…	7.2 ± 0.7	13.78 ± 0.04	11.2 ± 1.1
Si II	1260	248.8 ± 21.7	−50.3 ± 4.0	12.67 ± 0.14	12.2 ± 7.4
Si II	1193	194.5 ± 16.6	…	…	…
Si II	1190	134.2 ± 15.9	7.5 ± 1.8	13.60 ± 0.03	25.4 ± 2.6
Si II	1304	76.2 ± 19.9	…	…	…
C II	1334	449.4 ± 20.5	−4.3 ± 3.8	14.72 ± 0.04	49.8 ± 5.3
Si III	1206	496.2 ± 16.8	−53.2 ± 17.2	13.37 ± 0.29	29.8 ± 11.7
		…	3.1 ± 11.1	13.68 ± 0.24	28.9 ± 8.0
Si IV	1393	…	…	…	…
Si IV	1402	…	…	…	…
N V	1238	⩽61.8	…	⩽13.47	…
N V	1242	⩽46.2	…	…	…

Notes. Column (1): the species being measured. Column (2): the rest wavelength of the species in units of angstrom. Column (3): the measured rest-frame equivalent width (W) in units of milliangstrom. Column (4): the velocity centroid (v_{obs}) of the absorber in units of kilometers per second. Column (5): the log$N$ of the component in units of square centimeters. Column (6): the Doppler b parameter of the absorber in units of kilometers per second.
[a] Upper limits are 3 times the noise level within a 100 km s^{-1} range.
[b] An intervening absorber is present at the galaxy's systematic velocity, which we were unable to model and remove, so no upper limit measurement could be made.
[c] Intervening S II absorption profiles from the Milky Way were modeled and removed before the upper limit was measured.

(This table is available in its entirety in machine-readable form in the online article.)

of NGC 3344 caused the blueward component of its Lyα feature to be blended with the Milky Way's Lyα line. However, blending was not an issue for any of the metal features.

3. Results and Discussion

3.1. Absorber Kinematics

We looked for trends between the Doppler width of absorbers (b) with various galaxy properties in Table 1. A correlation between b and column density (log$N$) was observed in each ion except Si II, as shown in Figure 3. Smaller log$N$ values seem to give rise to narrower absorption features, while larger log$N$ values generally have wider features. Performing Kendall τ tests revealed that the trends in C II, Si III, and Si IV are statistically significant with τ values of 0.49, 0.61, and 0.43, with associated p-values of $\sim 10^{-4}$, $\sim 10^{-8}$, and $\sim 10^{-3}$, respectively. Si II, on the other hand, is consistent with no correlation ($\tau = 0.17$ and p-value $= 0.18$).

One explanation for this trend is that C II and Si III are more likely to be saturated than Si II and Si IV. Another explanation is the presence of unresolved, overlapping components appearing as a single component along sight lines probing closer to the galactic disk, similar to what has been seen in Mg II (e.g., G. G. Kacprzak et al. 2011; N. M. Nielsen et al. 2018). Of the 15 sight lines that showed Si IIλ1260 absorption, 12 had simultaneous detections in at least one of the weaker transitions ($\lambda\lambda$1193, 1190, 1304). This prevented the trend from emerging in the ion since the weaker lines allow us to resolve more components when the λ1260 line is saturated. However, for the Si IV ($\lambda\lambda$1393, 1402) and N V ($\lambda\lambda$1238, 1242) doublets, only the stronger transition was detected in 7 of 11 and 2 of 4 sight lines, respectively. Not having the weaker counterpart may have caused the trend to be present in these ions, though not as strongly as C II and Si III.

The largest (primary) components of Si II, C II, and Si III along each sight line, as measured by log$N$, tend to have velocity centroids (v_{obs}) within ± 100 km s^{-1} of the galaxy's v_{sys}. Meanwhile, the smaller (secondary) components are found as far away as -300 and 200 km s^{-1}. At distances farther from the galaxies (i.e., larger values of ρ) these ions produced few absorption features, implying that the cool CGM is more dense closer to galaxies than farther into the halo. We also find ions over a large range of ionization potentials (IPs), e.g., 13.6 eV for O I and 97.9 eV for N V, at the similar velocities, indicating kinematic alignment across multiple gas phases. However, it is possible that absorption from multiple phases that are kinematically aligned may not arise from the same process

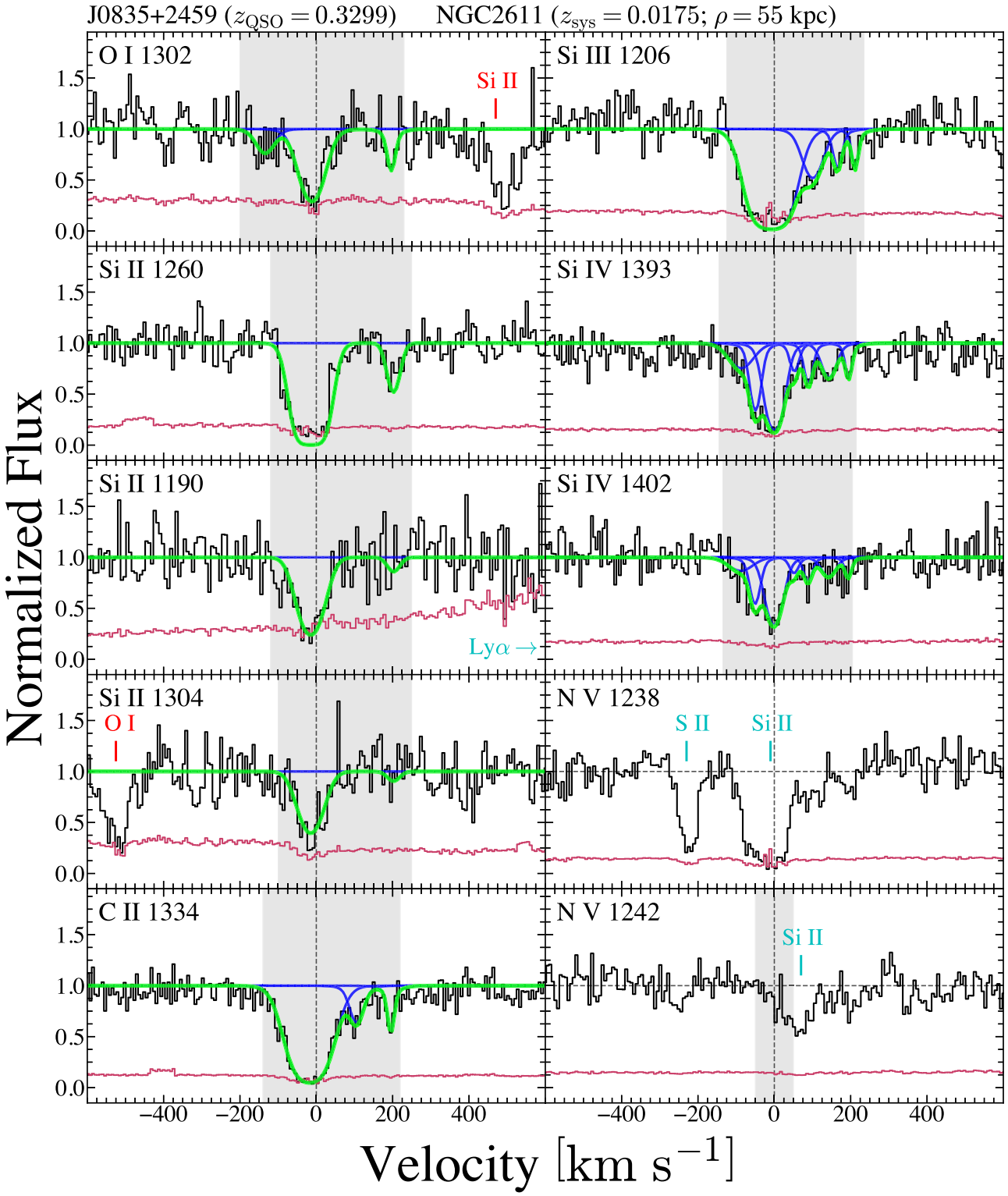

Figure 2. Voigt profile fits of the spectrum toward the QSO J0835+2459 probing the galaxy NGC 2611. Each panel is centered on the galaxy's systematic velocity (v_{sys}). Individual components are shown in blue, with the combined profile in green. The gray shaded regions show the range used to calculate the rest-frame equivalent width. Features other than the one being highlighted are colored based on their origin: cyan for Milky Way features, red for features associated with our target galaxy, yellow for those from the background QSO, and pink for intervening systems. The Si IIλ1193 Å transition is located within the Lyα emission line and so is not included in the fit or shown here. Similar figures are available for each QSO–galaxy pair.

(The complete figure set (30 images) is available in the online article.)

(T. J. Cooper et al. 2021; K. J. Haislmaier et al. 2021; Z. Qu et al. 2022).

The amount of motion along a sight line can be inferred by measuring the line-of-sight velocity dispersion. We define this measure as $\sigma_{LOS}^2 = \langle v^2 \rangle - \langle v \rangle^2$, where v represents the velocity centroid of the components and the angled brackets indicate taking the mean. Sight lines with a single component are excluded from this analysis. This measure has been shown

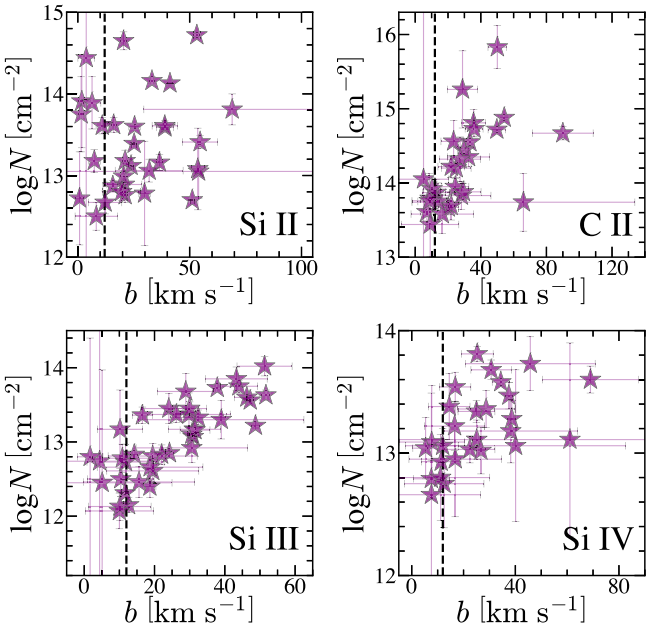

Figure 3. Measured Doppler width against column density for our most frequently detected ions. The ion being shown in each panel is indicated in the lower right corner. The vertical black dashed line indicates the resolution of the G130M filter of COS (FWHM $\approx$ 20 km s^{-1} corresponding to a $b \approx 12$ km s^{-1}). Components to the left of the line are likely unresolved. The strength of the correlation seems to be related to the number of available transitions. It is strongest for Si III and C II, which have a single transitions; weak for Si IV, which has two transitions; and not present for Si II, which has four transitions. C II and Si III are also more likely to be saturated than Si II and Si IV, which could also playing a role in causing this trend.

to trace the underlying turbulent velocities in the CGM on average (B. Koplitz et al. 2023). For our most frequently detected ions (Si II, C II, Si III, and Si IV), we show in Figure 4 the $\sigma_{\rm LOS}$ values as a function of ρ normalized by the galaxy's $R_{\rm vir}$ (left panel) and by $R_{\rm HI}$ (right panel). Most of the panels in the figure show anticorrelations, except for Si II when ρ is normalized by the galaxy's $R_{\rm HI}$. Kendall τ tests indicate that the correlations of Si II, Si III, and Si IV are not statistically significant. With C II, however, these tests show that the correlation is stronger when ρ is normalized by $R_{\rm HI}$, with $\tau = -0.48$ (p-value = 0.031), compared to $\tau = -0.33$ (p-value = 0.153) for $\rho/R_{\rm vir}$, respectively. The $\sigma_{\rm LOS}$ values we measure, as well as the radial decline out to $\sim$0.4 $R_{\rm vir}$, are similar to those derived from the Si II measurements of the COS-Halos survey (J. K. Werk et al. 2013) and the MAIHEM simulations (B. Koplitz et al. 2023).

The velocity centroids of our Voigt profile fits can also be used to determine how clustered the components are in velocity space. To constrain this, we performed a cross-correlation analysis between $v_{\rm obs}$ of Si II and C II against Si III. We compare to Si III since it is the most frequently detected ion in our sample. The generalized S. D. Landy & A. S. Szalay (1993) estimator was adopted, such that

$$x + 1 = \frac{(DD/n_{DD}) - 2(DR/n_{DR}) + (RR/n_{RR})}{(RR/n_{RR})}, \quad (1)$$

where DD refers to data–data matching, DR refers to data–random matching, and RR refers to random–random matching. Following N. Tejos et al. (2014) and C. W. Finn et al. (2016), each matching set was normalized, such that $n_{\rm DD} = N_{\rm real}(N_{\rm real}-1)/2$, $n_{\rm DR} = N_{\rm rand}(N_{\rm real})^2$, and $n_{\rm RR} = N_{\rm rand}N_{\rm real}(N_{\rm rand}N_{\rm real} - 1)/2$. Here, $N_{\rm real}$ and $N_{\rm rand}$ refer to the number of real and random absorbers, respectively, used in the analysis. The random samples were drawn from a uniform distribution between $\pm$600 km s^{-1}. Our uncertainties were estimated using a bootstrap analysis in which we randomly select sight lines, with replacements, and performed the same cross-correlation analysis. This was done 1000 times, with the 1σ width of this distribution adapted as our uncertainties. The results of this analysis are shown in Figure 5.

Comparing $v_{\rm obs}$(Si II) to $v_{\rm obs}$(Si III) in the top panel of Figure 5 shows a peak in the velocity separations at $\Delta v_{\rm obs} \leqslant 20$ km s^{-1}, with a decreasing trend out to $\sim$400 km s^{-1} with no pair of absorbers being found with further separations. There are three bins that are statistically significant at $\geqslant 3\sigma$: $\leqslant$20 km s^{-1}, 60–80 km s^{-1}, and 120–140 km s^{-1}. Performing this analysis between $v_{\rm obs}$(Si III) and $v_{\rm obs}$(C II), as shown in the bottom panel of Figure 5, finds a similar peak at $\Delta v_{\rm obs} \leqslant 20$ km s^{-1}, with an even sharper falloff. Similarly, no pair of absorbers were found with $\Delta v_{\rm obs} \gtrsim 400$ km s^{-1}. Three bins in this distribution are found to be statistically significant: $\leqslant$20 km s^{-1}, 60 –80 km s^{-1}, and 180–200 km s^{-1}. It is important to note that the noise dominates this analysis at velocity separations $\geqslant$200 km s^{-1} in both panels. Performing Kolmogorov–Smirnov tests between these distributions returned a p-value near 1, suggesting that these samples are not different at a statistically significant level.

When considering individual QSO–galaxy pairs, we find that galaxies with larger $M_\star$ and $M_{\rm halo}$ tend to have larger velocity separations. This could be indicative of virial support of the CGM gas.

A similar cross-correlation analysis was done by S. Borthakur et al. (2016) between the Lyα and Si III absorbers from the combined COS-Halos+COS-GASS sample. Their distribution followed a similar trend as those shown in Figure 5, with a peak in their lowest $\Delta v_{\rm obs}$ bin and a decline out to $\sim$400 km s^{-1}. However, they find a few systems with $\Delta v_{\rm obs} > 400$ km s^{-1}. The consistency between these analyses suggest that Lyα, Si II, C II, and Si III may be cospatial or tracing similar gas phases.

3.2. Metal Content and Equivalent Widths

We find that the sight lines that probe the CGM closer to the foreground galaxy, relative to both $R_{\rm vir}$ and $R_{\rm HI}$, have more components on average than those farther out. We show this distribution for $\rho/R_{\rm vir}$ in Figure 6. By considering the number of components of each ion along a sight line, we are able limit the impact that unresolved components and weak absorbers have on the individual distributions. We present the results of this in the far right panel of Figure 6. Similar to what was seen when considering each ion individually, there are more resolved components closer to the foreground galaxy. These distributions are not consistent from the radial density distribution of a Navarro–Frenk–White dark matter halo (J. F. Navarro et al. 1996), with $R_{\rm vir} = 213$ kpc and $M_{\rm vir} = 10^{11.8}$ $M_\odot$, the median values of the COS-DIISC sample. In addition, the distributions are not consistent with being produced by longer path lengths through a CGM of uniform density. It is important to note that we are comparing the shape of these distributions to the average number of

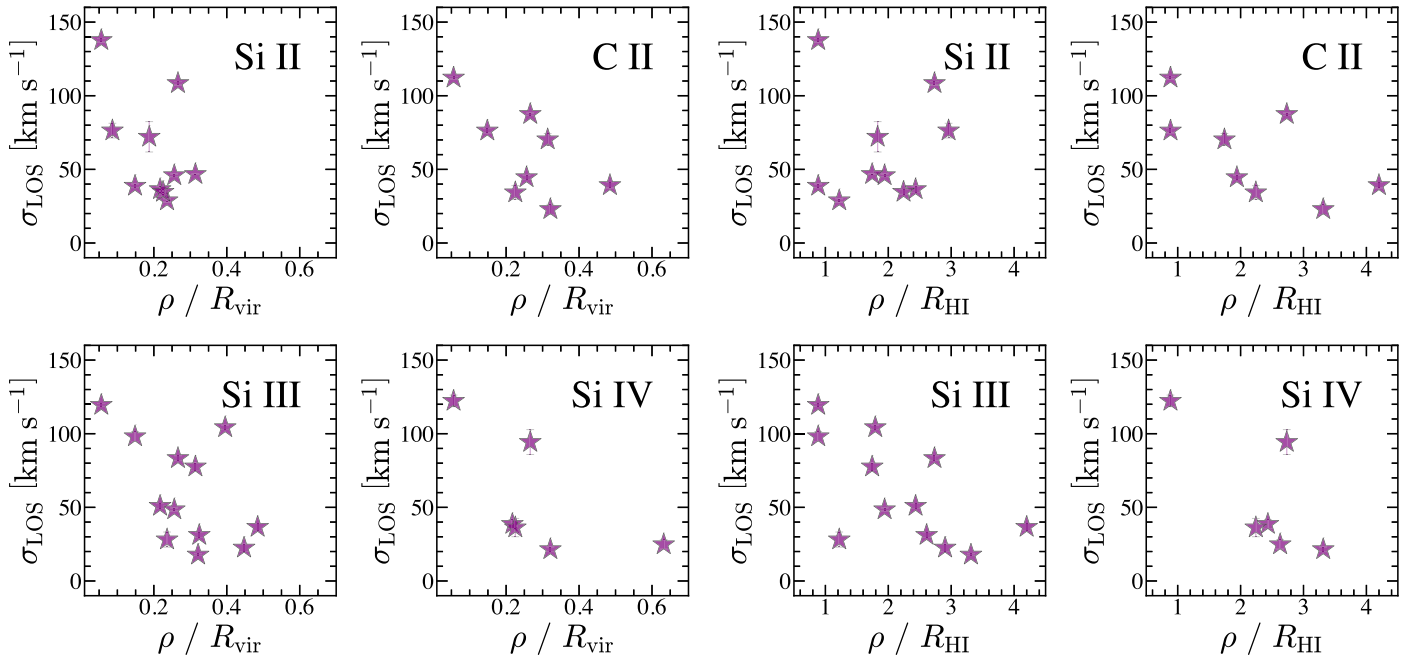

Figure 4. Inferred line-of-sight velocity dispersion as a function of impact parameter relative to the galaxy's virial radius (left) and the galaxy's H I radius (right) for the most frequently detected ions. The ion being shown in each panel is indicated in the upper right corner.

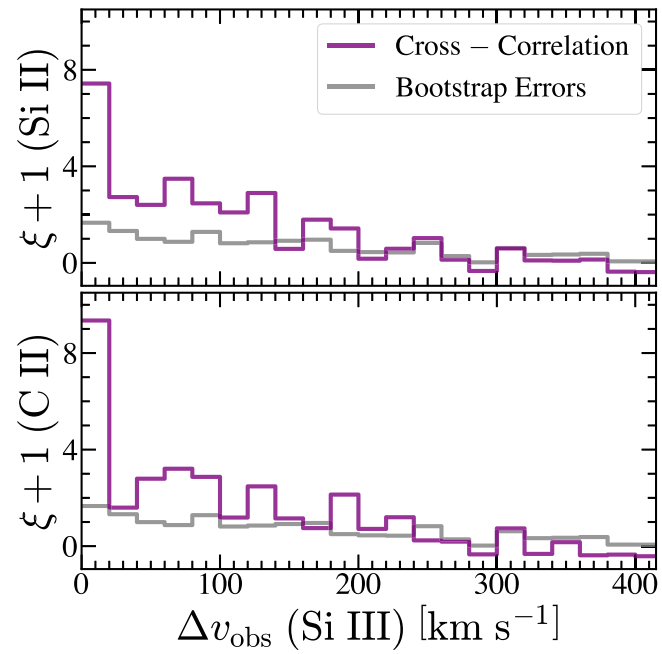

Figure 5. Cross-correlation analysis of Si III absorbers shown in purple with the standard deviation of our bootstrap analysis (as discussed in Section 3.1) in gray. The top panel compares the velocity centroids of Si II to those of Si III, while the bottom panel compares the centroids of C II to Si III.

components per sight line, not predicting the number of absorbing clouds they would produce.

Since the DIISC sample was selected based on the QSO's position relative to the galaxy's R_{HI}, we are able to determine the distribution of absorbers in terms of distance from the galaxy's H I disk. In the top panels Figure 7, we show the distribution of logW_r for Si II (left columns), C II (center columns), and Si III (right columns) as a function of ρ/R_{HI}. A clear anticorrelation emerges with sight lines closer to the H I disks tending to have larger logW_r values than farther away. It is noteworthy that all sight lines with Si III nondetections are found beyond $\sim$2.5 R_{HI}. Si II and C II, however, have a nondetection at $\rho \approx 1.8$ R_{HI} from the QSO–galaxy pair J1354+1441–KUG 1352+149 where Si III is detected. The Lyα and Si III measurements from the COS-GASS survey also produced anticorrelations with distance from the H I disk out to $\sim$30 R_{HI} (S. Borthakur et al. 2015). These show that the distance a QSO probes with respect to a galaxy's H I disk will largely dictate whether or not metals with low and medium IPs (13.6 eV $\leqslant$ IP $\leqslant$ 33.5 eV) are found along the sight line.

A similar radial decline was seen in the H I absorbers of MaNGA galaxies when looking at ρ relative to the galaxy's effective radius of the stellar disk (V. V. Klimenko et al. 2023). Our measurements of Si II, C II, and Si III display a similar trend with respect to the galaxy's r-band Petrosian radius ($R_{pet,r}$). We show these trends in the bottom panels of Figure 7. Unlike the relationships seen with respect to R_{HI}, the nondetections are found across the entire range of $\rho/R_{pet,r}$ for these ions. As a result, we conclude that the distance from a galaxy's H I disk is a better tracer of metals in the CGM.

With the COS-Halos and COS-GASS surveys covering a similar range of galactic parameters as we do in COS-DIISC, we can combine the samples to study global trends in the CGM. We look for trends between this combined sample with respect to ρ normalized by the galaxy's R_{vir} since the R_{HI} of COS-Halos galaxies are unknown. In Figure 8, we show logW_r of Si II (left) and Si III (right) as a function of ρ/R_{vir}. The foreground galaxies in each sample are separated into star-forming and passive galaxies based on their sSFRs (sSFR $\equiv$ SFR/$M_\star$) being above or below 10^{-11} yr^{-1}, respectively. The star-forming galaxies are shown as blue stars for COS-DIISC, light navy circles for COS-GASS, and cyan diamonds for COS-Halos, while passive galaxies are shown as red stars for COS-DIISC, orange circles for COS-GASS, and yellow diamonds for COS-Halos.

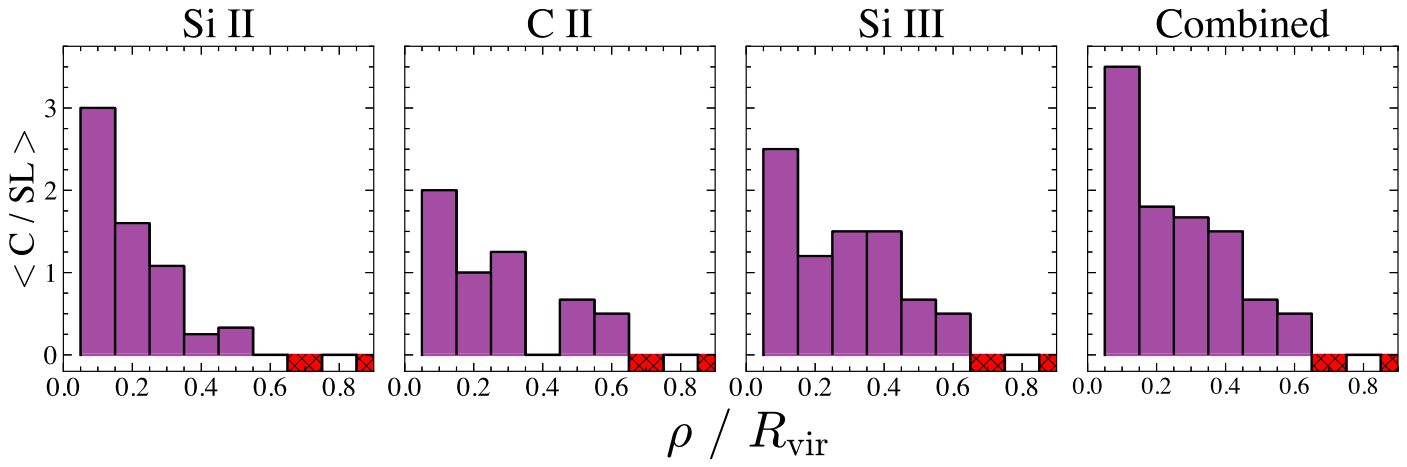

Figure 6. Histograms of the average number of components per sight line (<C/SL>) of Si II (far left), C II (left center), and Si III (right center) as a function of impact parameter normalized by the galaxy's virial radius. The far right panel is the number of components along a sight line determined by considering the Si II, C II, and Si III features together, as defined in the text. Bins that do not contain any sight lines are indicated by red hatching to distinguish them from bins in which no components were detected.

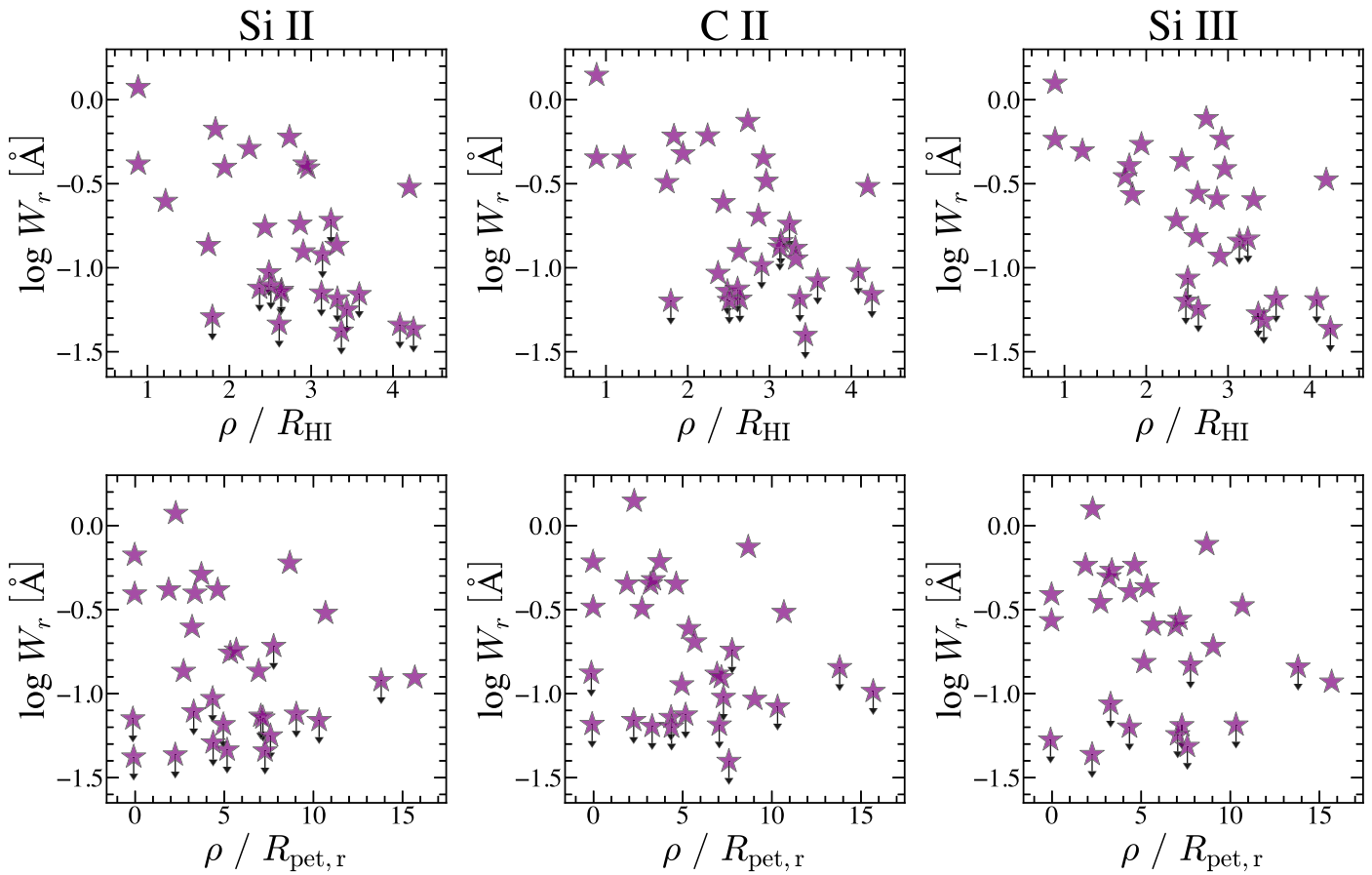

Figure 7. Measured rest-frame equivalent width of Si II (left column), C II (center column), and Si III (right column) as a function of impact parameter normalized by the galaxy's H I disk (top panels) and impact parameter normalized by the galaxy's *r*-band Petrosian radius (bottom panels). Upper limits are shown with a downward arrow.

Larger values of logW_r (i.e., stronger absorbers) are found closer to galaxies, similar to what we see in Figure 7. Beyond $\sim$0.4 $R_{\rm vir}$, no absorbers were detected with logW_r(Si II) > -0.5. This suggests that the outer halos of these galaxies contain weaker absorbing clouds than are found closer to the disk though this could be the result of difference in the density or ionization state of the gas. Figure 8 shows that few metals are detected beyond $\sim$0.7 $R_{\rm vir}$, consistent with previous studies (e.g., C. J. Liang & H.-W. Chen 2014; N. Lehner et al. 2015; Z. Qu et al. 2023). A similar radial decline was seen in the total silicon column density (N(Si) = N(Si II) + N(Si III) + N(Si IV)) for M31 (N. Lehner et al. 2020). The vast majority of upper limits of both ions have log$W_r < -1$. Similar trends have been found in Mg II

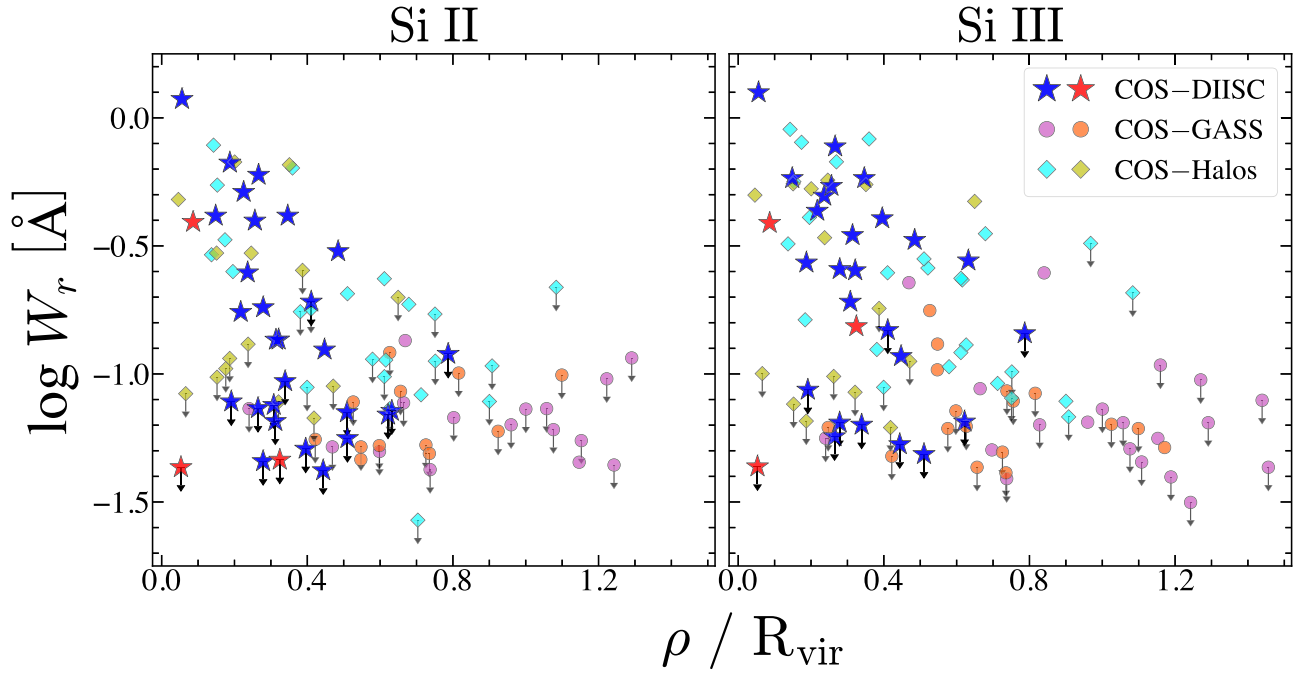

Figure 8. Measured rest-frame equivalent width of Si II (left) and Si III (right) as a function of impact parameter relative to the galaxy's virial radius. We show the different samples being plotted as different symbols with stars representing COS-DIISC points, circles showing COS-GASS, and diamonds for COS-Halos. Each sample is split into star-forming (shown in blue for COS-DIISC, light navy for COS-GASS, and cyan for COS-Halos) and passive (shown in red for COS-DIISC, orange for COS-GASS, and yellow for COS-Halos) galaxies as defined in Section 3.2. Upper limits are plotted with a downward arrow.

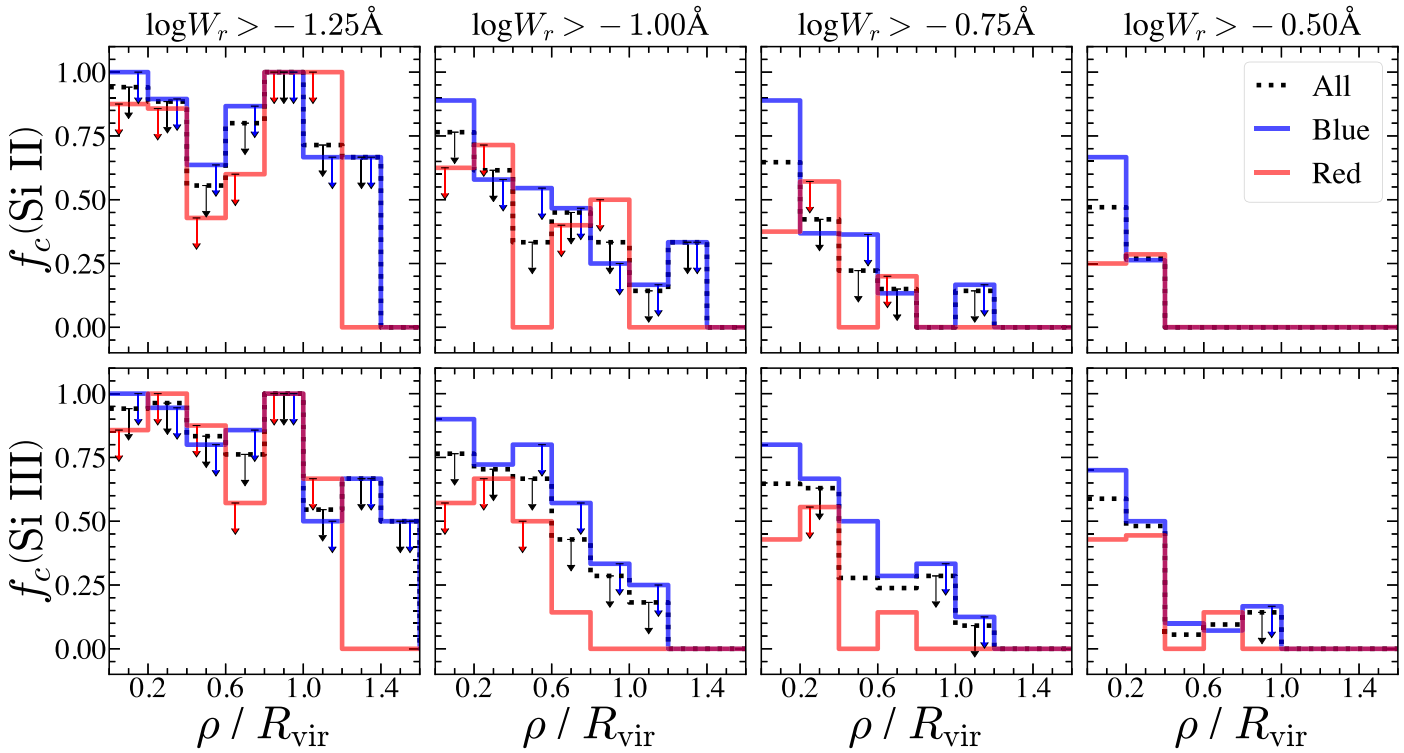

Figure 9. Covering fraction of Si II (top) and Si III (bottom) as a function of impact parameter relative to the galaxy's virial radius for the combined COS-DIISC +COS-GASS+COS-Halos sample. Each column uses a different log rest-frame equivalent width limit, which is shown at the top of the column. The star-forming galaxies are shown in blue, passive galaxies in red, and all galaxies in black. Bins that include upper limit rest-frame equivalent widths are shown with a downward arrow.

(e.g., H.-W. Chen et al. 2010; C. W. Churchill et al. 2013; N. M. Nielsen et al. 2013; S. H. Ho et al. 2017).

Comparing Figure 8 to the top panels of Figure 7 reveals an interesting trend. Nondetections (upper limits) are only found at $\rho \gtrsim 1.5\ R_{HI}$ in Figure 7, while they are found across the entire range of ρ/R_{vir} in Figure 8. The Lyα absorbers in the COS-DIISC sample produced a similar trend (S. Borthakur et al. 2024). This likely indicates that the radial profile of absorbers

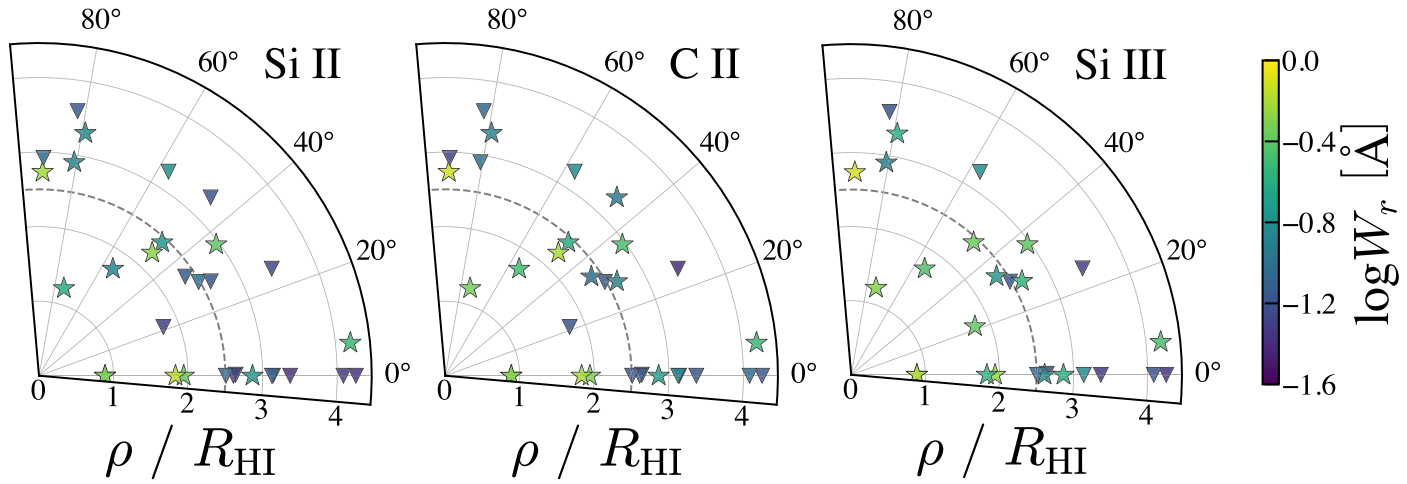

Figure 10. Position of QSO in terms of angle from the target galaxy's major axis and impact parameter relative to the galaxy's H I radius. Data points are colored based on the measured rest-frame equivalent width of Si II (left), C II (center), and Si III (right). Sight lines where the ion is detected are shown as stars, while those with nondetections are shown as downward triangles. Si III is detected in all sight lines within 2.5 $R_{\rm HI}$ as indicated by the dashed line and is seen in Figure 7.

Table 4
Input Parameters of CLOUDY PIE Models

QSO (1)	Galaxy (2)	$z_{\rm sys}$ (3)	Cold (4)	Cool (5)	Warm (6)	$\rho_{\rm MW}$ (7)	log$N$(H I) (8)
J0832+2431	KUG 0829+246B	0.0430	2	1	0	50	14.0–18.0
J0835+2459	NGC 2611	0.0175	2	3	3	50	15.0–19.8
J0917+2719	J0917+2720	0.0469	1	2	0	50	15.0–18.0
J1042+2501	NGC 3344	0.0020	1	1	1	50	14.0–18.0
J1043+1151	M95/NGC 3351	0.0026	1	1	1	10	14.0–18.0
J1124+1131	NGC 3666	0.0035	1	2	1	50	14.0–18.0
J1133+2423	NGC 3728	0.0232	2	2	0	100	14.0–18.0
J1140+1136	NGC 3810	0.0033	2	1	1	50	13.0–18.0
J1157+0906	AGC 213643	0.0367	0	1	1	100	14.0–18.0
J1157+1140	2MASXJ1157+1139	0.0213	0	1	1	50	14.0–18.0
J1221+0430	M61/NGC 4303	0.0052	2	5	3	50	14.0–20.0
J1314+2606	J1314+2605	0.0431	1	1	0	100	14.0–18.0
J1432+0955	NGC 5669	0.0046	1	0	0	10	14.0–20.0
J1524+0419	2MASXJ1524+0421	0.0374	1	2	0	100	14.0–18.0
J1533+1501	LEDA 140527	0.0429	1	1	0	10	15.0–21.0
J1558+1205	IC 1149	0.0156	1	1	0	50	14.0–18.0

Note. Columns (1) and (2): the QSO and galaxy, respectively, of the sight line. Column (3): the redshift of the system. Columns (4), (5), and (6): the number of cold, cool, and warm clouds, respectively, included in the analysis. Columns (7) and (8): the ρ of the Milky Way radiation field and the range of log$N$(H I) used in the analysis.

in the CGM is better traced by $\rho/R_{\rm HI}$ rather than $\rho/R_{\rm vir}$, which is typically used in CGM studies. In particular, this may show that the strength of absorbers in the inner CGM (radii $\lesssim$2.5 $R_{\rm HI}$) can largely be predicted by the size of the galaxy's H I disk.

We show the covering fraction (f_c) of Si II and Si III as a function of ρ normalized by $R_{\rm vir}$ in Figure 9. These were calculated for the combined COS-DIISC+COS-GASS+COS-Halos sample. Various logW_r cuts were used to look for trends with absorber strengths. Bins that include upper limit measurements of logW_r are shown with a downward arrow. Radial declines are seen in most cases, with star-forming galaxies typically having higher f_c values than passive galaxies. This has been also been seen in simulations (e.g., S. Appleby et al. 2021). As the logW_r cut is increased, we see the decline in f_c become steeper for both ions, which further indicates that the strongest absorbers tend to be found closer to galaxies. The high values within $R_{\rm vir}$ are similar to what was found by other studies (e.g., J. K. Werk et al. 2013; C. J. Liang & H.-W. Chen 2014; P. Richter et al. 2016; N. Lehner et al. 2020).

In Figure 10, we show the measured logW_r of Si II (left), C II (center), and Si III (right) as a function of ρ normalized by $R_{\rm HI}$ and the angle from the galaxy's major axis. We define galaxies with minor axis to major axis ratios greater than 0.8 to be face-on, and these sight lines are considered to be passing through the extended galactic disk. As a result, we set the orientation angle to 0° in the figure. As previously noted, stronger components of each ion are found closer to the disk of galaxies. However, no trends are seen between the orientation of the QSO relative to the galaxy's major axis and the strength of the CGM absorbers.

3.3. Ionization State

Comparing the N ratio of metals of different gas phase can reveal how ionized the gas is. Here, we analyze the ratios of the

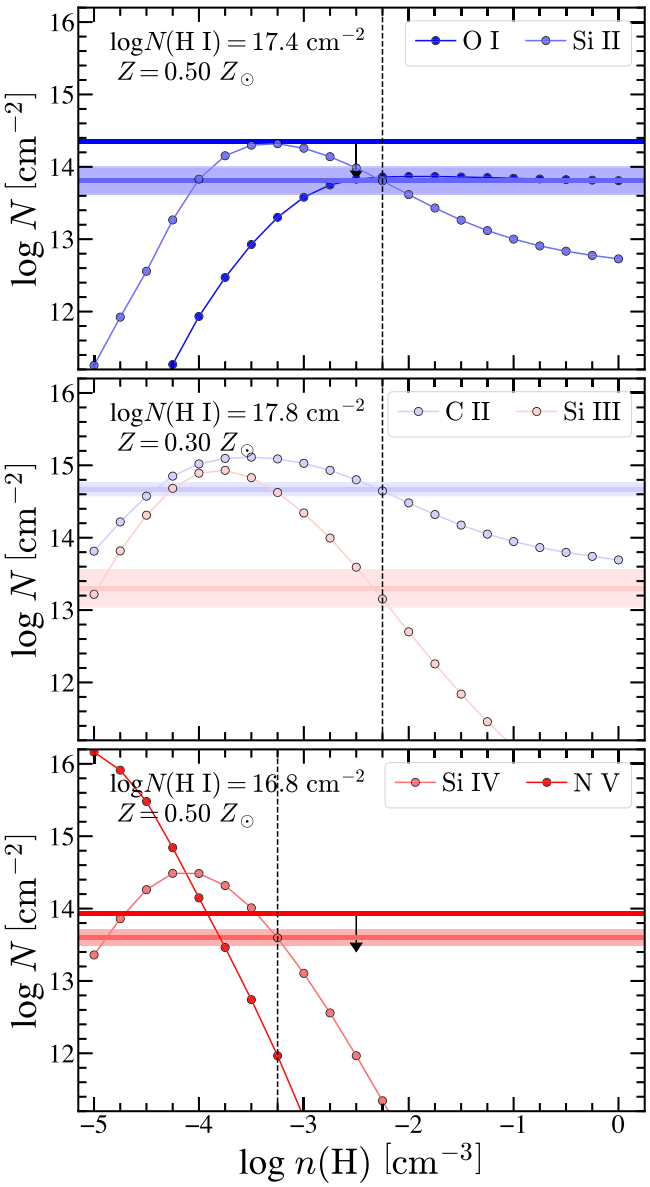

Figure 11. An example comparison of our measurements for the QSO–galaxy pair J1042+2501–NGC 3344 to CLOUDY PIE models. The top, middle, and bottom panels correspond to the cold, cool, and warm gas phases, respectively. Our measurements are shown as colored horizontal lines, with the shaded regions indicating the uncertainties. The color indicates the ion being plotted as shown in the upper right corner. The H I column density and metallicity of the model are shown in the upper left corner. The total H density that best reproduced the measurements is shown as vertical black dashed lines. Similar figures for each system included in this analysis are available.

(The complete figure set (29 images) is available in the online article.)

silicon ions we have access to (i.e., N(Si II)/N(Si III) and N(Si IV)/N(Si III)). While other metal line ratios can be used, such as N(Si III)/N(C II), we only analyze ions of silicon to limit the impact of dust depletion.

Most components had N(Si II)/N(Si III) and N(Si IV)/N(Si III) ratios near 1 though there is a rather large spread in each. No trends were seen between either ratio and the properties of the host galaxy in Table 1, suggesting that the galaxy itself has little impact on how ionized the CGM is. We note, however, that the galaxies in the DIISC survey are typical $L_\star$ galaxies, and so trends may appear when looking at very small ρ or around more extreme galaxies, such as starbursts. Below, we explore processes that could be driving the observed ionization states.

3.4. Ionization Equilibrium Models

The processes responsible for ionizing the CGM can be understood by comparing observed log$N$ values to those predicted from ionization models. To determine if our absorbers are in photoionization equilibrium (PIE), we compare our measurements to CLOUDY models (v.23; M. Chatzikos et al. 2023). We assume the ions we have access to fall into three phases: a cold phase traced by O I and Si II, a cool phase traced by C II and Si III, and a warm phase traced by Si IV and N V. This gives us 19 cold phase components, 25 cool phase components, and 12 warm phase components to include in this analysis. The results presented here are intended to be an initial constraint on the prevalence of PIE at the disk–CGM interface. A more detailed analysis will be performed in a future study.

Each CLOUDY model is exposed to a F. Haardt & P. Madau (2012) extragalactic UV background as well as the Milky Way radiation field. We use the Milky Way radiation fields presented in A. J. Fox et al. (2005), which are generated at ρ = 10, 50, and 100 kpc. For each sight line, we select the radiation field with the ρ value that is closest to the one listed in Column (7) of Table 1. The total H density of the CLOUDY models was varied from log[n(H)/cm^3] = −5.00 to 0.00 in steps of 0.25 dex. A robust measure of log$N$(H I) was difficult for most sight lines since the Lyα features were saturated and we do not have access to other lines in the Lyman series. As a result, we ran CLOUDY over a range of values for log$N$(H I) in steps of 0.2 dex based on the measurements presented in S. Borthakur et al. (2024). Similarly, the metallicity along our sight lines is poorly constrained due to the lack of multiple Lyman series lines, leading us to assume metallicities of 0.04, 0.30, 0.50, and 1.00 times the solar value (M. Asplund et al. 2009) motivated by other CGM surveys (N. Lehner et al. 2013; J. X. Prochaska et al. 2017). Table 4 presents the input parameters used in our CLOUDY modeling. This analysis is shown in Figure 11 for the QSO–galaxy pair J1042+2501–NGC 3344 as an example. Similar figures are available for each sight line included in this analysis.

It is important to highlight the limitations of this analysis. Even though the CGM has been shown to contain multiple gas phases (e.g., J. K. Werk et al. 2013; T. J. Cooper et al. 2021; K. J. Haislmaier et al. 2021; Sameer et al. 2024), a clear delineation between the phases, as we are presenting, is unrealistic. A single ion, such as Si III or Si IV, could be produced by multiple phases, which we do not account for here. The Milky Way radiation fields included in the models is a constant source of photons, but this could vary with time. While we are assuming solar relative abundances (M. Asplund et al. 2009), there is evidence that these can vary in galaxies and their CGM (e.g., A. J. Fox et al. 2004; Y. I. Izotov et al. 2023). It is known that some metals in the CGM of galaxies may be locked in dust and molecules; however, we are assuming there is no depletion in our measurements for this analysis. As shown in Figure 3, the largest absorbers, particularly of C II and Si III, are saturated and could be the result of components overlapping in velocity space. The impact all of these have on the results presented below will be explored in a future study.

Table 5
Best-fit CLOUDY Models

Cold Phase				Cool Phase				Warm Phase			
Z (1)	log n(H) (2)	log$N$(H I) (3)	Length (4)	Z (5)	log n(H) (6)	log$N$(H I) (7)	Length (8)	Z (9)	log n(H) (10)	log$N$(H I) (11)	Length (12)
J0832+2431 at $z_{sys} = 0.0430$											
1.00	−0.50	17.0	0.2	…	…	…	…	…	…	…	…
[a]	[a]	[a]	[a]	1.00	−2.75	17.0	844.5	…	…	…	…
J0835+2459 at $z_{sys} = 0.0175$											
[a]	[a]	[a]	[a]	1.00	−3.25	17.0	6355.3	0.50	−3.00	19.8	40793.4
…	…	…	…	1.00	−3.25	15.8	415.4	1.00	−2.75	17.2	1061.5
0.50	0.00	17.6	0.2	1.00	−3.00	15.8	137.7	0.30	−2.75	17.4	2010.6
J0917+2719 at $z_{sys} = 0.0469$											
1.00	−2.50	17.8	1001.2	1.00	−3.00	17.0	2360.3	…	…	…	…
…	…	…	…	1.00	−3.25	16.0	734.0	…	…	…	…
J1042+2501 at $z_{sys} = 0.0020$											
0.50	−2.25	17.4	248.4	0.30	−2.25	17.8	468.2	0.50	−3.25	16.8	6634.3
J1043+1151 at $z_{sys} = 0.0026$											
0.50	−2.00	17.4	88.7	0.50	−2.75	17.0	1140.2	[a]	[a]	[a]	[a]
J1124+1131 at $z_{sys} = 0.0035$											
1.00	−0.50	17.4	0.3	1.00	−3.25	16.0	627.9	…	…	…	…
…	…	…	…	0.04	−2.75	17.2	1537.7	0.50	−3.25	16.4	1956.9
J1133+2423 at $z_{sys} = 0.0232$											
0.30	−2.00	16.8	18.2	0.04	−2.50	17.2	432.3	…	…	…	…
1.00	−2.25	17.4	150.7	0.30	−2.75	17.0	788.9	…	…	…	…
J1140+1136 at $z_{sys} = 0.0033$											
1.00	−1.25	17.2	2.5	0.30	−2.50	17.2	482.2	[a]	[a]	[a]	[a]
0.50	−0.50	17.6	0.6	…	…	…	…	…	…	…	…
J1157+0906 at $z_{sys} = 0.0367$											
…	…	…	…	0.50	−3.25	16.4	1968.6	0.50	−3.75	15.8	4871.1
J1157+1140 at $z_{sys} = 0.0213$											
…	…	…	…	[a]	[a]	[a]	[a]	0.50	−3.75	16.0	8787.7
J1221+0430 at $z_{sys} = 0.0052$											
…	…	…	…	[a]	[a]	[a]	[a]	0.50	−4.00	16.0	41580.4
…	…	…	…	0.50	−2.75	16.2	214.2	…	…	…	…
…	…	…	…	0.50	−2.25	16.4	35.7	1.00	−4.50	15.0	49839.3
…	…	…	…	0.30	−2.50	16.6	191.7	…	…	…	…
1.00	−2.25	18.6	904.7	[a]	[a]	[a]	[a]	0.50	−4.25	16.0	151816.4
1.00	−0.75	18.2	4.0	…	…	…	…	…	…	…	…
J1314+2606 at $z_{sys} = 0.0431$											
0.30	0.00	17.6	0.2	0.30	−3.75	15.6	3618.9	…	…	…	…
J1432+0955 at $z_{sys} = 0.0046$											
1.00	−1.75	18.2	86.5	…	…	…	…	…	…	…	…
J1524+0419 at $z_{sys} = 0.0374$											
0.30	−2.25	17.6	271.6	1.00	−3.00	16.8	1274.3	…	…	…	…
…	…	…	…	0.50	−2.75	16.4	197.7	…	…	…	…
J1533+1501 at $z_{sys} = 0.0429$											
1.00	−2.25	18.0	708.1	0.30	−2.50	17.4	1352.6	…	…	…	…

Table 5
(Continued)

Cold Phase				Cool Phase				Warm Phase			
Z (1)	log n(H) (2)	log$N$(H I) (3)	Length (4)	Z (5)	log n(H) (6)	log$N$(H I) (7)	Length (8)	Z (9)	log n(H) (10)	log$N$(H I) (11)	Length (12)
J1558+1205 at $z_{sys} = 0.0156$											
0.50	−0.75	18.0	2.6	0.30	−2.75	17.0	863.0	…	…	…	…

Notes. Columns (1), (5), and (9): the best-fit metallicity of the cold, cool, and warm phases, respectively, in units of solar metallicity ($Z_\odot$). Columns (2), (6), and (10) show the best-fit log n(H) of the models in units of cubic centimeters. Columns (3), (7), and (11): the best-fit log$N$(H I) in units of square centimeters. Columns (4), (8), and (12): the resulting cloud lengths in units of parsecs. Ellipses are used to indicate where a gas phase could not be constrained.
[a] This component does not match CLOUDY PIE models.

(This table is available in its entirety in machine-readable form in the online article.)

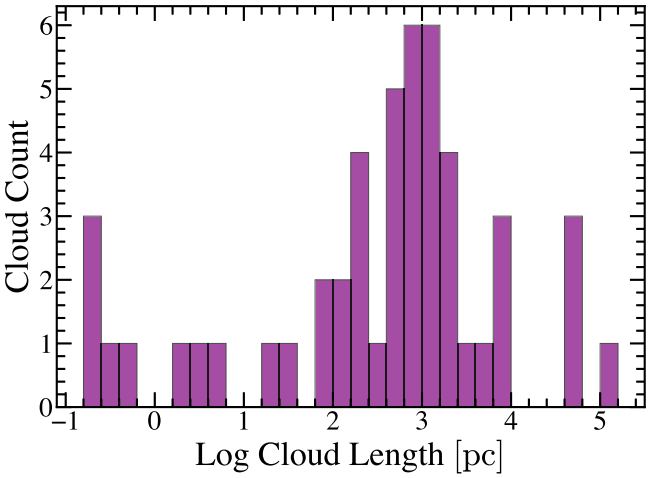

Figure 12. Derived cloud lengths based on CLOUDY models.

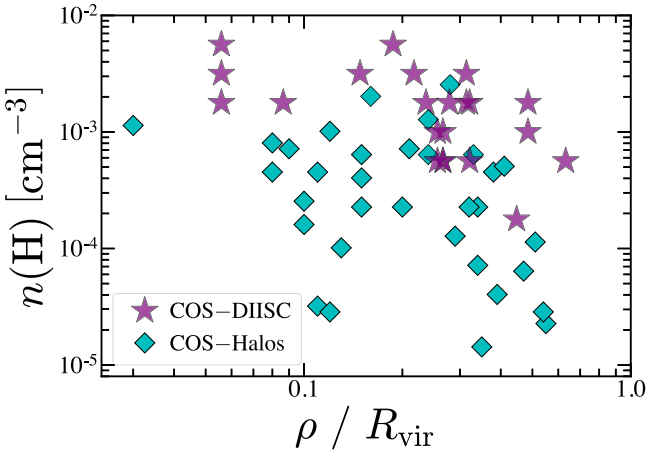

Figure 13. Inferred total hydrogen density as a function of impact parameter normalized by the galaxies virial radius. Values from the cool clouds in our sample (COS-DIISC) are shown as purple stars, while those from the COS-Halos sample are shown as cyan diamonds.

We present the results of this analysis in Table 5. The majority of these absorbers (17 of 19 cold phase clouds, 22 of 25 cool phase clouds, and 10 of 12 warm phase clouds) are consistent with PIE models though we cannot rule out photoionization taking place in the remaining systems. The

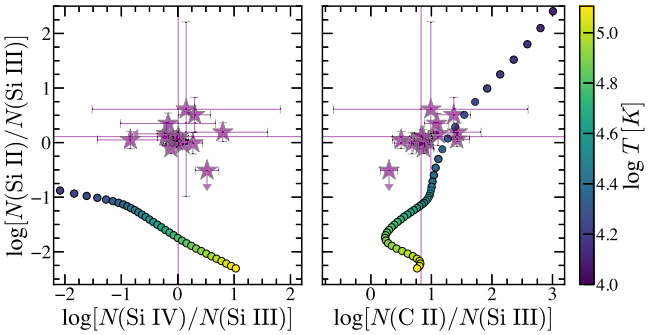

Figure 14. Comparing CIE models from O. Gnat & A. Sternberg (2007; colored circles), to observed column density ratios (stars). The color of the circles corresponds to the temperature of the CIE model.

cold components, which are consistent with PIE, were found to have log[n(H)/cm^3] between −2.50 and 0.00 with temperatures between $T \approx 10^{3.5}$ and $10^{4.0}$ K. The cool components were found to have log[n(H)/cm^3] between −3.75 and −2.25 with temperatures between $T \approx 10^{3.8}$ and $10^{4.1}$ K. The warm components had log[n(H)/cm^3] between −4.50 and −2.75 with temperatures between $T \approx 10^{3.9}$ and $10^{4.1}$ K.

We show the distribution of the cloud lengths in Figure 12. The cloud length can be determined as N(H)/n(H). We use the N(H) from the model, such that N(H) = N(H I) + N(H II). All of the cold phase clouds were found to be $\lesssim$1 kpc in length. The cool phase clouds were all smaller than 7 kpc in length though most (19/22) were smaller than 2 kpc. Meanwhile, all of the warm phase clouds were larger than 1 kpc though the majority (6/10) are smaller than 10 kpc. These sizes should be thought of as upper limits given that at least some of the absorbers with the largest N are likely comprised of many smaller clouds overlapping in velocity space and we do not have the spectral resolution to resolve each cloud individually. These sizes are similar to the clouds derived by the CUBS collaboration (F. S. Zahedy et al. 2021) as well as those inferred by B. A. Keeney et al. (2017) but are smaller than those from the COS-Halos survey (J. K. Werk et al. 2014, 2016). This consistency between surveys suggest these lengths are characteristic cloud lengths in the CGM regardless of the phase being probed. As discussed above, the analysis presented is intended to be a first pass at modeling our measurement. A more detailed study will be implemented in a future study.

In Figure 13, we plot the n(H) values inferred from the CLOUDY models for our cool clouds as a function of ρ

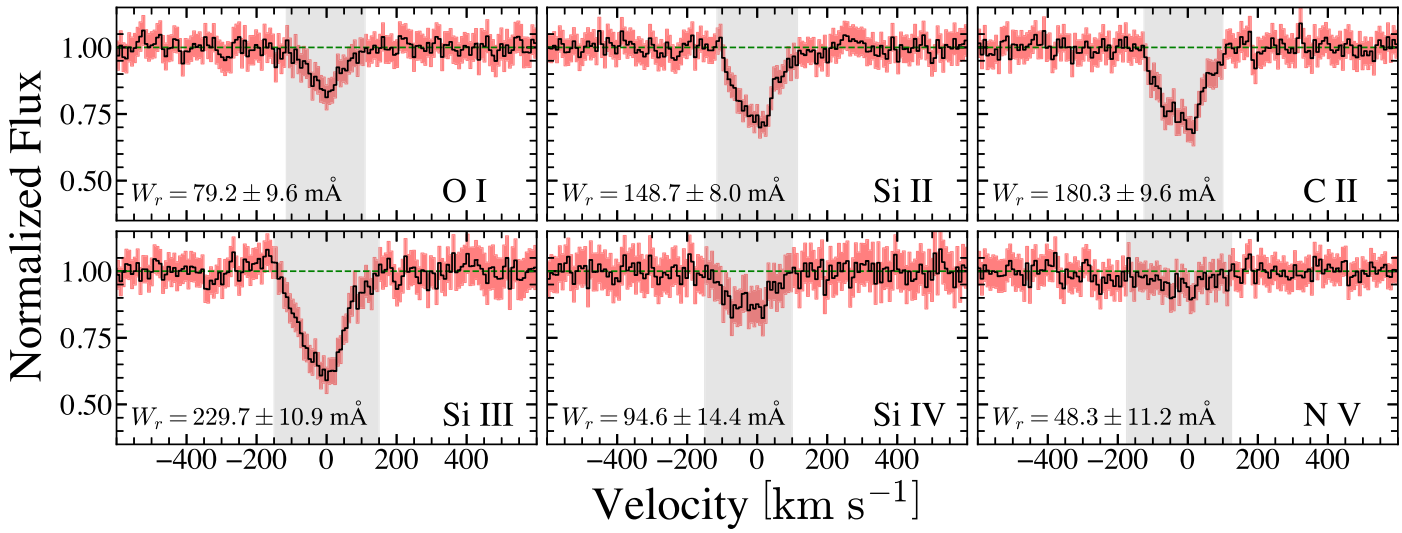

Figure 15. Stacked spectra of all sight lines at the velocity of each ion. The metal being shown is indicated in the bottom right of each panel. The 1σ uncertainties are shown as red shaded regions. The gray regions highlight the velocity range used to calculate the rest-frame equivalent width of the spectra, which we show in the bottom left corner in units of milliangstrom.

normalized by $R_{\rm vir}$. We also plot the values from COS-Halos (J. K. Werk et al. 2014) for comparison. We only show the results for the cool clouds to better compare to the COS-Halos sample. Both of these samples show a similar distribution.

To determine whether the components along our sight lines are in collisional ionization equilibrium (CIE), we compare our metal line ratios to the solar metallicity models from O. Gnat & A. Sternberg (2007), which are shown in Figure 14. The left panel compares the different ionization states of silicon we have access to, which covers a range of IPs (16.4–45.1 eV), while the right panel probes more coherent phases covering a narrower range of IPs (16.4–33.5 eV). In the right panel, many of our points are consistent with CIE at $T \approx 10^{4.4}$–$10^{4.5}$ K; however, they do not match our measurements shown in the left panel of the figure. These show that low-ion components are likely not in CIE though we are not able to conclusively rule this out. Though the high-ion components of Si IV and C IV could be in CIE, there can be different ionization mechanisms for different phases of gas. Similar to the PIE analysis above, this is intended to be an initial constraint on whether our measurements could be explained using CIE models. We will explore these models in more detail in a future study to robustly determine the role collisional ionization plays in our measurements.

3.5. Stacking Spectra

To study the average properties of the CGMs in our sample rather than individual systems, we stack our spectra at the $v_{\rm sys}$ of the host galaxy. For ions with multiple transitions, we only stack the strongest transitions. The results of this stacking is shown in Figure 15. All of the ions show absorption features above our 3σ detection limit.

Si III has the largest absorption, as measured by W_r, of any ion, followed by C II. The depth of the stacked absorbers are independent constraints on the f_c of ions. The O I, Si IV, and N V spectra are relatively shallow, leading to $f_c < 20\%$. Si II, C II, and Si III, meanwhile, had f_c between 30% and 41%, similar to what was found at $\sim R_{\rm vir}$ in Figure 9.

We constrained the $v_{\rm obs}$ of these stacked spectra using the apparent optical depth method (B. D. Savage & K. R. Sembach 1991). The $v_{\rm obs}$ of each stack is within ± 25 km s^{-1}, indicating that most of the absorption is occurring at or near the galaxy's $v_{\rm sys}$.

These trends suggest that the most prominent gas phase, of those we have access to, in the CGM at low z is the cool-warm phase, as traced by C II and Si III, and that most of the absorption is taking place at a similar velocity as the host galaxy. However, it is important to note that the z of our sample galaxies prevent us from studying metals with higher IPs such as O VI and Ne VIII with COS.

4. Summary and Conclusions

Here, we have investigate the content, kinematics, and ionization of UV metal absorption lines in the CGM surrounding 31 galaxies ($z_{\rm sys}$ = 0.0020–0.0507) from the DIISC survey using HST/COS spectra. The selection criteria of the DIISC survey allow us to determine the impact that a galaxy's H I disk has on its CGM as never before. The main conclusions of our analysis are as follows:

1. Of the ions under study, Si III was detected most frequently along the sight lines, with 18 of 31 galaxies (∼55%) showing at least one component. The vast majority of these (13; ∼77%) showed multicomponent structures. All ions showed fewer components per sight line on average when probing the CGM at larger ρ.
2. We find stronger absorbers (i.e., larger logW_r) of each ion closer to the disk of galaxies. The majority of sight lines within ∼2.5 $R_{\rm HI}$ contained metals, while those beyond this were more likely to be nondetections. These results indicate that the radial profile of the metal ions with IPs between 13.6 eV and 33.5 eV are more correlated with $\rho/R_{\rm HI}$, rather than the $\rho/R_{\rm vir}$ measure typically used by CGM surveys.
3. In most ions, a strong correlation is seen between the Doppler b parameters and log$N$ of individual components. When taken with the above points, this trend can be explained by many unresolved, overlapping components appearing as one large component near the galaxy's $v_{\rm sys}$, suggesting clustering of clouds close to the galaxy's $v_{\rm sys}$.

4. Many of our components were consistent with PIE models from CLOUDY regardless of the gas phase being probed. This suggests that photoionization is the dominate ionization process near the disk–CGM interface. These models reveal that our components probing the cold gas phase are produced by clouds with lengths $\lesssim$1 kpc. The cool gas phase was largely produced by clouds smaller than 2 kpc in length. Meanwhile, the majority of the components probing the warm gas phase were smaller than 10 kpc in length. No low-ion components were found to be consistent with CIE models though we cannot rule out the high-ion absorbers being in CIE. It is important to note that this analysis is intended to be a first pass at modeling our measurements using PIE and CIE models. A more detailed analysis of these will be explored in a future study.

These results allow us to further study the distribution of CGM gas around low-z galaxies and constrain models that can reproduce the trends. We will explore this fully in a future publication.

Acknowledgments

We thank the referee for constructive comments, which helped improve the robustness and clarity of the manuscript. B.K., S.B., M.P., T.M., and T.H. are supported by HST grant No. HST-GO-14071 administrated by STScI, which is operated by AURA under contract NAS 5-26555 from NASA, and NSF grants 2108159 and 2009409. S.B., and M.P. are supported by NASA ADAP grant No. 80NSSC21K0643.

B.K. would like to thank the Oases in the Cosmic Desert 2023 CGM conference for inspiring some of the analysis presented in this work. B.K., S.B., M.P., T.M., and T.H. acknowledge the native people and the land that Arizona State University's campuses are located on in the Salt River Valley, the ancestral territories of Indigenous peoples, including the Akimel O'odham (Pima) and Pee Posh (Maricopa) Indian Communities, whose care and keeping of these lands allows us to be here today.

Facilities: HST (COS); Sloan.

Software: `matplotlib` (v3.2.2; J. D. Hunter 2007), `astropy` (v4.2.1; Astropy Collaboration et al. 2013, 2018), `CLOUDY` (v.23; M. Chatzikos et al. 2023), `numpy` (v1.22.0; C. R. Harris et al. 2020), `scipy` (v1.6.2; P. Virtanen et al. 2020), `pandas` (v1.3.5; J. Reback et al. 2021).

ORCID iDs

Brad Koplitz https://orcid.org/0000-0001-5530-2872
Sanchayeeta Borthakur https://orcid.org/0000-0002-2724-8298
Timothy Heckman https://orcid.org/0000-0001-6670-6370
Mansi Padave https://orcid.org/0000-0002-3472-0490
Tyler McCabe https://orcid.org/0000-0002-5506-3880
Jason Tumlinson https://orcid.org/0000-0002-7982-412X
Andrew J. Fox https://orcid.org/0000-0003-0724-4115

References

Appleby, S., Davé, R., Sorini, D., Storey-Fisher, K., & Smith, B. 2021, MNRAS, 507, 2383
Asplund, M., Grevesse, N., Sauval, A. J., & Scott, P. 2009, ARA&A, 47, 481
Astropy Collaboration, Price-Whelan, A. M., Sipőcz, B. M., et al. 2018, AJ, 156, 123
Astropy Collaboration, Robitaille, T. P., Tollerud, E. J., et al. 2013, A&A, 558, A33
Behroozi, P. S., Conroy, C., & Wechsler, R. H. 2010, ApJ, 717, 379
Bordoloi, R., Tumlinson, J., & Werk, J. K. 2014, ApJ, 796, 136
Borthakur, S., Heckman, T., Tumlinson, J., et al. 2015, ApJ, 813, 46
Borthakur, S., Heckman, T., Tumlinson, J., et al. 2016, ApJ, 833, 259
Borthakur, S., Padave, M., Heckman, T., et al. 2024, arXiv:2409.12554
Bowen, D. V., Chelouche, D., Jenkins, E. B., et al. 2016, ApJ, 826, 50
Burchett, J. N., Tripp, T. M., Prochaska, J. X., et al. 2019, ApJL, 877, L20
Burchett, J. N., Tripp, T. M., Wang, Q. D., et al. 2018, MNRAS, 475, 2067
Chatzikos, M., Bianchi, S., Camilloni, F., et al. 2023, RMxAA, 59, 327
Chen, H.-W., Helsby, J. E., Gauthier, J.-R., et al. 2010, ApJ, 714, 1521
Chen, H. W., Prochaska, J. X., & Lanzetta, K. M. 2002, in ASP Conf. Ser. 254, Extragalactic Gas at Low Redshift, ed. J. S. Mulchaey & J. T. Stocke (San Francisco, CA: ASP), 88
Chen, H.-W., Zahedy, F. S., Boettcher, E., et al. 2020, MNRAS, 497, 498
Churchill, C. W., Trujillo-Gomez, S., Nielsen, N. M., & Kacprzak, G. G. 2013, ApJ, 779, 87
Cooper, T. J., Rudie, G. C., Chen, H.-W., et al. 2021, MNRAS, 508, 4359
Danforth, C. W., & Shull, J. M. 2008, ApJ, 679, 194
Davies, J. J., Crain, R. A., Oppenheimer, B. D., & Schaye, J. 2020, MNRAS, 491, 4462
Decataldo, D., Shen, S., Mayer, L., Baumschlager, B., & Madau, P. 2023, arXiv:2306.03146
Dekel, A., & Birnboim, Y. 2006, MNRAS, 368, 2
Dekel, A., Birnboim, Y., Engel, G., et al. 2009, Natur, 457, 451
Donahue, M., & Voit, G. M. 2022, PhR, 973, 1
Faucher-Giguère, C.-A., Feldmann, R., Quataert, E., et al. 2016, MNRAS, 461, L32
Finn, C. W., Morris, S. L., Tejos, N., et al. 2016, MNRAS, 460, 590
Fox, A. J., Savage, B. D., Wakker, B. P., et al. 2004, ApJ, 602, 738
Fox, A. J., Wakker, B. P., Savage, B. D., et al. 2005, ApJ, 630, 332
Gim, H. B., Borthakur, S., Momjian, E., et al. 2021, ApJ, 922, 69
Giovanelli, R., Haynes, M. P., Kent, B. R., et al. 2005, AJ, 130, 2598
Gnat, O., & Sternberg, A. 2007, ApJS, 168, 213
Green, J. C., Froning, C. S., Osterman, S., et al. 2012, ApJ, 744, 60
Haardt, F., & Madau, P. 2012, ApJ, 746, 125
Hafen, Z., Stern, J., Bullock, J., et al. 2022, MNRAS, 514, 5056
Haislmaier, K. J., Tripp, T. M., Katz, N., et al. 2021, MNRAS, 502, 4993
Harris, C. R., Millman, K. J., van der Walt, S. J., et al. 2020, Natur, 585, 357
Haynes, M. P., Giovanelli, R., Kent, B. R., et al. 2018, ApJ, 861, 49
Heckman, T., Borthakur, S., Wild, V., Schiminovich, D., & Bordoloi, R. 2017, ApJ, 846, 151
Ho, S. H., Martin, C. L., Kacprzak, G. G., & Churchill, C. W. 2017, ApJ, 835, 267
Hunter, J. D. 2007, CSE, 9, 90
Izotov, Y. I., Schaerer, D., Worseck, G., et al. 2023, MNRAS, 522, 1228
Kacprzak, G. G., Churchill, C. W., Evans, J. L., Murphy, M. T., & Steidel, C. C. 2011, MNRAS, 416, 3118
Kauffmann, G., Borthakur, S., & Nelson, D. 2016, MNRAS, 462, 3751
Keeney, B. A., Stocke, J. T., Danforth, C. W., et al. 2017, ApJS, 230, 6
Keeney, B. A., Stocke, J. T., Rosenberg, J. L., et al. 2013, ApJ, 765, 27
Kereš, D., Katz, N., Weinberg, D. H., & Davé, R. 2005, MNRAS, 363, 2
Klimenko, V. V., Kulkarni, V., Wake, D. A., et al. 2023, ApJ, 954, 115
Koplitz, B., Edward Buie, I., & Scannapieco, E. 2023, ApJ, 956, 54
Landy, S. D., & Szalay, A. S. 1993, ApJ, 412, 64
Lehner, N., Berek, S. C., Howk, J. C., et al. 2020, ApJ, 900, 9
Lehner, N., Howk, J. C., Tripp, T. M., et al. 2013, ApJ, 770, 138
Lehner, N., Howk, J. C., & Wakker, B. P. 2015, ApJ, 804, 79
Liang, C. J., & Chen, H.-W. 2014, MNRAS, 445, 2061
Machado, R. E. G., Tissera, P. B., Lima Neto, G. B., & Sodré, L. 2018, A&A, 609, A66
Meyer, M. J., Zwaan, M. A., Webster, R. L., et al. 2004, MNRAS, 350, 1195
Muzahid, S., Fonseca, G., Roberts, A., et al. 2018, MNRAS, 476, 4965
Navarro, J. F., Frenk, C. S., & White, S. D. M. 1996, ApJ, 462, 563
Nelson, D., Sharma, P., Pillepich, A., et al. 2020, MNRAS, 498, 2391
Nielsen, N. M., Churchill, C. W., & Kacprzak, G. G. 2013, ApJ, 776, 115
Nielsen, N. M., Kacprzak, G. G., Pointon, S. K., Churchill, C. W., & Murphy, M. T. 2018, ApJ, 869, 153
Osterman, S., Green, J., Froning, C., et al. 2011, Ap&SS, 335, 257
Padave, M., Borthakur, S., Gim, H. B., et al. 2021, ApJ, 923, 199
Padave, M., Borthakur, S., Gim, H. B., et al. 2024a, ApJ, 960, 24
Padave, M., Borthakur, S., Jansen, R. A., et al. 2024b, arXiv:2407.16690
Péroux, C., & Howk, J. C. 2020, ARA&A, 58, 363

Prochaska, J. X., Werk, J. K., Worseck, G., et al. 2017, ApJ, 837, 169
Qu, Z., Chen, H.-W., Rudie, G. C., et al. 2022, MNRAS, 516, 4882
Qu, Z., Chen, H.-W., Rudie, G. C., et al. 2023, MNRAS, 524, 512
Rafelski, M., et al. 2018, COS Data Handbook, 4 (Baltimore, MD: STScI)
Reback, J., Jbrockmendel, McKinney, W., et al. 2021, pandas-dev/pandas: Pandas v1.3.5, Zenodo, doi:10.5281/zenodo.5774815
Richter, P., Wakker, B. P., Fechner, C., et al. 2016, A&A, 590, A68
Rigby, J. R., Charlton, J. C., & Churchill, C. W. 2002, ApJ, 565, 743
Rudie, G. C., Steidel, C. C., Trainor, R. F., et al. 2012, ApJ, 750, 67
Sameer, Charlton, J. C., Wakker, B. P., et al. 2024, MNRAS, 530, 3827
Savage, B. D., & Sembach, K. R. 1991, ApJ, 379, 245
Shen, S., Madau, P., Aguirre, A., et al. 2012, ApJ, 760, 50
Somerville, R. S., & Davé, R. 2015, ARA&A, 53, 51
Sorini, D., Davé, R., & Anglés-Alcázar, D. 2020, MNRAS, 499, 2760
Stocke, J. T., Keeney, B. A., Danforth, C. W., et al. 2013, ApJ, 763, 148
Suresh, J., Bird, S., Vogelsberger, M., et al. 2015, MNRAS, 448, 895
Swaters, R. A., van Albada, T. S., van der Hulst, J. M., & Sancisi, R. 2002, A&A, 390, 829
Tchernyshyov, K., Werk, J. K., Wilde, M. C., et al. 2023, ApJ, 949, 41
Tejos, N., Morris, S. L., Finn, C. W., et al. 2014, MNRAS, 437, 2017
Thom, C., Tumlinson, J., Werk, J. K., et al. 2012, ApJL, 758, L41
Tumlinson, J., Peeples, M. S., & Werk, J. K. 2017, ARA&A, 55, 389
Tumlinson, J., Thom, C., Werk, J. K., et al. 2011, Sci, 334, 948
Tumlinson, J., Thom, C., Werk, J. K., et al. 2013, ApJ, 777, 59
van de Voort, F., Springel, V., Mandelker, N., van den Bosch, F. C., & Pakmor, R. 2019, MNRAS, 482, L85
Veilleux, S., Cecil, G., & Bland-Hawthorn, J. 2005, ARA&A, 43, 769
Virtanen, P., Gommers, R., Oliphant, T. E., et al. 2020, NatMe, 17, 261
Voit, G. M., Bryan, G. L., Prasad, D., et al. 2020, ApJ, 899, 70
Werk, J. K., Prochaska, J. X., Cantalupo, S., et al. 2016, ApJ, 833, 54
Werk, J. K., Prochaska, J. X., Thom, C., et al. 2013, ApJS, 204, 17
Werk, J. K., Prochaska, J. X., Tumlinson, J., et al. 2014, ApJ, 792, 8
Wilde, M. C., Werk, J. K., Burchett, J. N., et al. 2021, ApJ, 912, 9
Zahedy, F. S., Chen, H.-W., Cooper, T. M., et al. 2021, MNRAS, 506, 877
Zinger, E., Pillepich, A., Nelson, D., et al. 2020, MNRAS, 499, 768
Zwaan, M. A., Meyer, M. J., Webster, R. L., et al. 2004, MNRAS, 350, 1210